A simplified atmospheric boundary layer model for an improved representation of air-sea interactions in eddying oceanic models: implementation and first evaluation in $\mathrm{NEMO(4.0)}$

Florian Lemarié[1], Guillaume Samson[2], Jean-Luc Redelsperger[3], Hervé Giordani[4], Théo Brivoal[2], and Gurvan Madec[5,1]

[1]Univ. Grenoble Alpes, Inria, CNRS, Grenoble INP, LJK, 38000 Grenoble, France
[2]Mercator Océan, Toulouse, France
[3]Univ. Brest, CNRS, IRD, Ifremer, Laboratoire d'Océanographie Physique et Spatiale (LOPS), IUEM, Brest, France
[4]Centre National de Recherches Météorologiques (CNRM), Université de Toulouse, Météo-France, CNRS, Toulouse, France
[5]Sorbonne Universités (UPMC, Univ Paris 06)-CNRS-IRD-MNHN, LOCEAN Laboratory, Paris, France

Correspondence: Florian Lemarié (florian.lemarie@inria.fr)

Abstract. A simplified model of the Atmospheric Boundary Layer (ABL) of intermediate complexity between a bulk parameterization and a three-dimensional atmospheric model is developed and integrated to the Nucleus for European Modelling of the Ocean (NEMO) general circulation model. An objective in the derivation of such simplified model called ABL1d is to reach an apt representation in ocean-only numerical simulations of some of the key processes associated to air/sea interactions

5 at the characteristic scales of the oceanic mesoscale. In this paper we describe the formulation of the ABL1d model and the strategy to constrain this model with large-scale atmospheric data available from reanalysis or real-time forecasts. A particular emphasis is on the appropriate choice and calibration of a turbulent closure scheme for the atmospheric boundary layer. This is a key ingredient to properly represent the air/sea interaction processes of interest. We also provide a detailed description of the NEMO-ABL1d coupling infrastructure and its computational efficiency. The resulting simplified model is then tested

10 for several boundary-layer regimes relevant to either ocean/atmosphere or sea-ice/atmosphere coupling. The coupled system is also tested with a realistic $0.25°$ resolution global configuration. The numerical results are evaluated using standard metrics from the literature to quantify the wind/sea surface temperature (a.k.a. thermal feedback effect), wind/currents (a.k.a. current feedback effect) and ABL/sea-ice couplings. With respect to these metrics, our results show very good agreement with observations and fully coupled ocean-atmosphere models for a computational overhead of about 9% in term of elapsed time

15 compared to standard uncoupled simulations. This moderate overhead, largely due to I/O operations, leaves room for further improvement to relax the assumption of horizontal homogeneity behind ABL1d and thus to further improve the realism of the coupling while keeping the flexibility of ocean-only modelling.

1 Introduction

Owing to advances in computational power, global oceanic models used for research or operational purposes are now config-

20 ured with increasingly higher horizontal/vertical resolution thus resolving the baroclinic deformation radius in the tropics (e.g.

Deshayes et al., 2013; Metzger et al., 2014; von Schuckmann et al., 2018). Meanwhile fine-scale local models are routinely used to simulate submeso-scales, which occur on scales on the order of $0.1 - 20 \, \mathrm{km}$ horizontally, and their impact on larger scales (e.g. Marchesiello et al., 2011; McWilliams et al., 2019). By increasing the oceanic model resolution, small scales features are explicitly resolved but an apt representation of the associated processes requires the relevant scales to be present also

25 in the surface forcings. Historically, Oceanic General Circulation Models (OGCMs) were forced by specified wind-stress and thermal boundary condition (from observations or reanalysis) independent from the oceanic state thus often leading to important drifts in model sea surface properties. To minimize such drifts, a flux correction in the form of a restoring of sea-surface temperature and salinity toward climatological values can be added (e.g. Haney, 1971; Barnier et al., 1995). To overcome the shortcomings of the forcing with specified flux, Takano et al. (1973) proposed to use a parameterization of the atmospheric

30 surface layer (ASL) constrained by large scale meteorological data and by the sea-state (essentially the sea-surface temperature and sometimes the surface currents) to compute the turbulent components of air-sea fluxes. Currently, whatever the target applications, such technique is widely used in the absence of a concurrently running atmospheric model. Such parameterization of the ASL (known as bulk parameterization, e.g. Beljaars, 1995; Large, 2006; Brodeau et al., 2017; Pelletier et al., 2018), which corresponds to a generalization of the classical neutral wall law to stratified conditions (Monin and Obukhov, 1954), is

35 expected to be valid in the first tenth of meters in the atmosphere. In practice, unless a fully coupled ocean-atmosphere model is used, atmospheric quantities at 10 meters, either from existing numerical simulations of the atmosphere or from observations, are prescribed as input to the bulk parameterization. Throughout the paper, this approach will be referred to as "ASL forcing strategy". A problem with such methodology is that the fast component of the system (the atmosphere) is specified to force the slow component (the ocean) whereas the inertia is in the latter. Indeed, a change in wind-stress or heat flux will affect 10 meter

40 winds and temperature more strongly than sea surface currents and temperature. In the "ASL forcing strategy", the key marine atmospheric boundary layer (MABL) processes are not taken into account and thus feedback loops between the MABL and the upper-ocean are not represented. An increasing number of studies based either on observational studies and/or on air-sea coupled simulations have unambiguously shown the existence of air-sea interactions at oceanic mesoscales (e.g. Giordani et al., 1998; Chelton and Xie, 2010; Frenger et al., 2013; Schneider and Qiu, 2015; Oerder et al., 2016). With particular relevance

45 for the present study, SST-induced changes in the stratification produce significant changes of wind speed and turbulent fluxes throughout the MABL, with an increase (resp. decrease) in wind speed over warm water (resp. cold water). As the wind blows over warm water, the MABL becomes more unstable and the associated increased vertical mixing enhances the downward mixing of momentum from the upper atmosphere to the near surface resulting in stronger surface winds (e.g. Wallace et al., 1989). Even if this coupling mainly occurs at oceanic eddy scales, this ocean forcing at small scales can induce significant

50 effects at larger scales by strengthening the turbulence in regions with large SST gradients (Hogg et al., 2009; Bryan et al., 2010). Besides the modulation of MABL turbulence, often referred to as downward momentum mixing mechanism, the SST-induced adjustment of the atmospheric pressure gradient is also thought to be an important mechanism (Lindzen and Nigam, 1987; Minobe et al., 2008; Lambaerts et al., 2013). Identifying the relative importance of each mechanism on the momentum balance is difficult because it depends on the dynamical regime and on the spatial and temporal scales of interest (Schneider

55 and Qiu, 2015; Ayet and Redelsperger, 2019; Redelsperger et al., 2019).

The momentum exchange between the ocean and the atmosphere is not only affected by a thermal coupling but also largely by a dynamical coupling through the dependence of surface wind-stress on oceanic surface currents (Dewar and Flierl, 1987; Renault et al., 2016b; Oerder et al., 2018) and by the surface wave state (e.g. Cavaleri et al., 2012). We, however, do not include this latter effect in the present study (this point will be discussed further in Sec. 6). The dynamical coupling has also

60 been shown to have significant upscaling effect at larger scale (Renault et al., 2016a).

It is obvious that the representation of the downward momentum mixing mechanism can not be accurately represented when large-scale atmospheric data are prescribed at 10 meters as in the ASL forcing strategy. Indeed the SST-induced stratification changes in the MABL is ignored, although a small fraction of this effect is accounted for through the modification of surface drag coefficient depending on the ASL stability (Businger and Shaw, 1984). Regarding the oceanic currents feedback on wind-

65 stress, the oceanic currents dependence in the surface stress results in a drag exerted by the air-sea interface on the ocean, analogous to the bottom-drag, Dewar and Flierl (1987) called this effect "top-drag", which leads to a reduction of the wind power input to the oceanic circulation. Renault et al. (2016b) showed that this reduction of wind power input is systematically over-estimated in uncoupled oceanic simulations compared to air-sea coupled simulations. A simulation that neglects the MABL adjustment to the current feedback can not represent the partial re-energization of the ocean and hence overestimates

70 the top-drag effect by more than 30% (e.g. Renault et al., 2016b, 2019a). The ASL forcing strategy used in most oceanic models will thus over-estimate the dynamical coupling and under-estimate the thermal coupling.

The various aspects discussed so far suggest that a relevant coupling at the characteristic scales of the oceanic mesoscales requires nearly the same horizontal resolution in the ocean and the atmosphere (since the atmosphere must "see" oceanic eddies and fronts) as well as an atmospheric component more complete than a simple ASL parameterization to estimate air-sea fluxes.

75 This assessment raises numerous questions on current practices to force oceanic models across all scales[1] in the absence of an interactive atmospheric model. The computational cost associated to the systematic use of fully coupled ocean atmosphere models of similar horizontal resolution is generally unaffordable and comes with practical issues like the proper definition of initial conditions (e.g. Mulholland et al., 2015) and the proper choice of a parameterization set. Moreover, in the fully coupled case at basin or global interannual scales the temporal consistency with the observed variability is generally lost unless a

80 nudging toward observations or reanalysis is done in the atmosphere above the MABL (e.g. Bielli et al., 2009). There is thus clearly room for improvement in the methodology to compute the surface boundary conditions for an ocean model. Alternatives to the ASL forcing strategy have been suggested by Seager et al. (1995) and Deremble et al. (2013). They proposed a vertically integrated thermodynamically active but dynamically passive MABL model where the wind and the MABL height are specified as in the current practices. By construction such model can not reproduce the various aforementioned coupling mechanisms

85 affecting the surface wind stress. Their focus is on the improvement of the large-scale thermodynamics while ours is on the improvement of the eddy-scale momentum exchanges.

The objective of the present study is to introduce a simplified model of the MABL of intermediate complexity between a bulk parameterization and a full three-dimensional atmospheric model and to describe its integration to the Nucleus for

---

[1]This remark is supported by the conclusions of the CLIVAR Working Group on Model Development following the Kiel meeting in Apr. 2014 http://www.clivar.org/sites/default/files/documents/exchanges65_0.pdf

European Modelling of the Ocean (NEMO) general circulation model (Madec, 2012). This approach will be referred to as "ABL

90   coupling strategy". A constraint in the conception of such a simplified model is to allow an apt representation of the downward momentum mixing mechanism and partial re-energization of the ocean by the atmosphere while keeping the computational efficiency and flexibility inherent to ocean only modeling. The paper is organized as follows. In Sec. 2, we describe the continuous formulation of the simplified model called ABL1d, including the parameterization scheme used to represent vertical turbulent mixing in the MABL and the strategy to constrain this model with large-scale atmospheric conditions. Sec. 3 provides

95   the description of the dicretization and of the practical implementation of the ABL1d model in the NEMO framework. In Sec. 4 and 5 numerical results obtained for some atmosphere-only simplified test-cases available in the literature and for a coupled NEMO- ABL1d simulation in a global configuration are shown. Finally, our conclusions and perspectives are summarized and discussed in Sec. 6.

2   Model equations

100 ### 2.1   Motivations and proposed approach

Global oceanic models can be run at higher resolution that global atmospheric models because of their affordable computational cost. From an oceanic perspective, we generally simulate at high-resolution (in space and time) ocean fields $\phi_{\mathrm{HR}}^{\mathrm{oce}}(x,y,z,t)$ over a time interval $t \in [0,T]$ over which only large scale atmospheric data $\phi_{\mathrm{LS}}^{\mathrm{atm}}(x,y,z,t)$ are known from the integration of a model $\mathcal{M}_{\mathrm{atm}}$ using lower-resolution surface oceanic data $\phi_{\mathrm{LS}}^{\mathrm{oce}}(x,y,z=0,t)$ to compute its surface boundary conditions, namely

105 $$\phi_{\mathrm{LS}}^{\mathrm{atm}}(x,y,z,t) = \mathcal{M}_{\mathrm{atm}}(\phi_{\mathrm{LS}}^{\mathrm{oce}}(x,y,z=0,t)), \qquad t \in [0,T]$$

Instead of directly using $\phi_{\mathrm{LS}}^{\mathrm{atm}}(x,y,z=10\,\mathrm{m},t)$ to constrain the oceanic model as in the ASL forcing strategy, our objective is to estimate (without running the full atmospheric model again) the correction to the $10\,\mathrm{m}$ large-scale atmospheric data associated both with the fine resolution in the oceanic surface fields and with the two-way air-sea coupling. Somehow we aim at finding a methodology to get a cheap estimate $\widetilde{\phi}_{\mathrm{HR}}^{\mathrm{atm}}(x,y,z=10\,\mathrm{m},t)$ of the solution that would have been obtained using

110 a coupling of $\mathcal{M}_{\mathrm{atm}}$ and the oceanic model at high resolution. To do so we could imagine several approaches: *(i)* estimate $\frac{\partial \mathcal{M}_{\mathrm{atm}}}{\partial \phi_{\mathrm{LS}}^{\mathrm{oce}}}$ (i.e. the derivatives of the atmospheric solution with respect to the oceanic parameters) via sensitivity analysis which would require to have the possibility to operate $\mathcal{M}_{\mathrm{atm}}$; *(ii)* Build a surrogate model via learning strategies which would require a huge amount of data and computing time; *(iii)* Select the feedback loops of interest and define a simplified model to mimic the underlying physical mechanisms. Following the terminology of Razavi et al. (2012), the first two approaches enter the

115 class of statistical or empirical data-driven models emulating the original model responses while the third one enters the class of low-fidelity physically-based surrogates which are built on a simplified version of the original system of equations. In the present study we consider this latter approach, in the spirit of Giordani et al. (2005) who derived a simplified oceanic model by degenerating the primitive equations system and prescribing geostrophic currents into the momentum equation in substitution of the horizontal pressure gradient. In this model, a simple 1D oceanic mixed layer is three-dimensionalized via advective

120 terms to couple the vertical columns with each other. The idea here is to translate this idea to the MABL context. Our approach

has some similarities with the diagnostic meteorological model CALMET (Scire et al., 2000) based on objective analysis. Using a wind field given by observations and/or a large scale model as an initial guess as well as fine resolution land-use and topography data, CALMET generates a new wind field which accounts for small scale processes like slope flows or terrain blocking effects, among other things. In our case the model will be prognostic and will be specialized for overwater conditions.

125 In the rest of this section we describe the continuous formulation of our simplified MABL model which will be referred to as ABL1d.

2.2 Formulation of a single column approach

The formulation of the ABL1d model is derived under the following assumptions: (*i*) horizontal homogeneity (i.e. $\partial_x \cdot = \partial_y \cdot = 0$), (*ii*) the atmosphere in the computational domain is transparent (i.e. $\partial_z \mathcal{I} = 0$ with $\mathcal{I}$ the radiative flux) meaning that cloud

130 physics is ignored and solar radiation and precipitations at the air-sea interface are specified as usual from observations (e.g. Large and Yeager, 2009) (*iii*) vertical advection is neglected. Such assumptions prevent the model to prognostically account for the SST-induced adjustment of the atmospheric horizontal pressure gradient and for horizontal advective processes associated with a higher resolution boundary condition at the air-sea interface. The focus here is on the proper representation of the modulation of the MABL turbulent mixing by the air-sea feedback which is thought to be the main coupling mechanism

135 at the characteristic scales of the oceanic mesoscales impacting $\phi^{\mathrm{atm}}(z = 10\,\mathrm{m}, t)$ hence air-sea fluxes. This mechanism is expected to explain most of the eddy-scale wind-SST and wind-currents interactions and is key to properly downscale large-scale atmospheric data produced by a coarse resolution GCM to the oceanic resolution.

At a given location in space, the ABL1d model for the Reynolds-averaged profiles of horizontal velocities $\mathbf{u}_h(z,t)$, potential temperature $\theta(z,t)$, and specific humidity $q(z,t)$, provided a suitable initial condition, is

$$
140 \quad
\begin{cases}
\partial_t \mathbf{u}_h &= -f\mathbf{k} \times \mathbf{u}_h + \partial_z\left(K_m \partial_z \mathbf{u}_h\right) + \mathbf{R}_{\mathrm{LS}} \\
\partial_t \theta &= \partial_z\left(K_s \partial_z \theta\right) + \lambda_s(\theta_{\mathrm{LS}} - \theta) \\
\partial_t q &= \partial_z\left(K_s \partial_z q\right) + \lambda_s(q_{\mathrm{LS}} - q)
\end{cases}
\tag{1}
$$

for the height z between a lower boundary z_{sfc} and an upper boundary z_{top} which will be considered horizontally constant because only the ocean and sea-ice covered areas are of interest. In (1), $\mathbf{k} = (0,0,1)^t$ is a vertical unit vector, f the Coriolis parameter, K_m and K_s are the eddy diffusivity respectively for momentum and scalars, the subscript LS is used to characterize large-scale quantities known a priori, $\lambda_s(z,t)$ is the inverse of a relaxation timescale, and $\mathbf{R}_{\mathrm{LS}}$ denotes a large-scale forcing for

145 the momentum equation. $\mathbf{R}_{\mathrm{LS}}$ can either represent a forcing by geostrophic winds $\mathbf{u}_G$ (i.e. $\mathbf{R}_{\mathrm{LS}} = f\mathbf{k} \times \mathbf{u}_G$) or equivalently by a horizontal pressure gradient (i.e. $\mathbf{R}_{\mathrm{LS}} = \left(\frac{1}{\rho_a}\boldsymbol{\nabla}_h p\right)_{\mathrm{LS}}$) combined with a standard Newtonian relaxation (i.e. $\mathbf{R}_{\mathrm{LS}} = \lambda_m(\mathbf{u}_{\mathrm{LS}} - \mathbf{u}_h)$). Because of the simplifications made to derive the ABL1d model the $\mathbf{R}_{\mathrm{LS}}$ term and a nonzero λ_s are necessary to prevent the prognostic variables to drift very far away from the large-scale values used to "guide" the model. By itself a relaxation term does not represent directly any real physical process, but the rationale is that it accounts for the influence of large-scale three-

150 dimensional circulation processes not explicitly represented in a simple 1d model. Note that this methodology is currently used to evaluate GCM parameterizations in 1D column model. Once the turbulent mixing and the Coriolis term have been computed

to provide a provisional prediction $\phi^{n+1,\star}$ at time $n+1$ for any ABL1d prognostic variable ϕ, the relaxation term provides a weighting between this prediction and the large-scale quantities

$$\phi^{n+1} = \Delta t \lambda \, \phi_{\text{LS}} + (1 - \Delta t \lambda)\phi^{n+1,\star} \tag{2}$$

155 with Δt the increment of the temporal discretization. Above the boundary layer, the ABL1d formulation is unable to properly represent the physics, therefore the λ parameter should be large while in the first tens of meters near the surface we expect the ABL1d model to accurately represent the interaction with the fine resolution oceanic state and thus the relaxation toward ϕ_{LS} should be small. The exact form of the λ_s and λ_m coefficients is discussed later in Sec. 2.4. Note that because of the relaxation term, three-dimensional atmospheric data for $\mathbf{u}_{\text{LS}}$, θ_{LS}, q_{LS}, and possibly $\left(\frac{1}{\rho_a}\boldsymbol{\nabla}_h p\right)_{\text{LS}}$ sampled between z_{sfc} and z_{top} must

160 be provided to the oceanic model instead of the two-dimensional data (usually at $10\,\text{m}$) necessary for an ASL forcing strategy. Since the ABL1d model does not include any representation of radiative processes and microphysics, the radiative fluxes and precipitation at the air-sea interface are similar to the one provided for a standard uncoupled oceanic simulation. The model requires boundary conditions for the vertical mixing terms which are computed via a standard bulk formulation:

$$K_m \partial_z \mathbf{u}_h|_{z=z_{\text{sfc}}} \quad = \quad C_D \|\mathbf{u}_h(z_{\text{sfc}}) - \mathbf{u}_{\text{oce}}\|(\mathbf{u}_h(z_{\text{sfc}}) - \mathbf{u}_{\text{oce}}), \tag{3}$$

165
$$K_s \partial_z \phi|_{z=z_{\text{sfc}}} \quad = \quad C_\phi \|\mathbf{u}_h(z_{\text{sfc}}) - \mathbf{u}_{\text{oce}}\|(\phi(z_{\text{sfc}}) - \phi_{\text{oce}}), \qquad \text{with } \phi = \theta, q \tag{4}$$

For the sake consistency, it is preferable to use a bulk formulation as close as possible to the one used to compute the three-dimensional large-scale atmospheric data $\phi_{\text{LS}}^{\text{atm}}$. Because in the present study the plan is to use a large-scale forcing from ECMWF reanalysis products, we use the IFS[2] bulk formulation such as implemented in the AeroBulk[3] package (Brodeau et al., 2017) to compute C_D, C_θ, and C_q in realistic simulations (see Sec. 5). Note that for an ASL forcing strategy $\mathbf{u}_h(z_{\text{sfc}})$

170 and $\phi(z_{\text{sfc}})$ in (3) would be respectively equal to $\mathbf{u}_{\text{LS}}(z = 10\,\text{m})$ and $\phi_{\text{LS}}(z = 10\,\text{m})$ while in the ABL coupling strategy those variables are provided prognostically by an ABL1d model. As far as the boundary conditions at $z = z_{\text{top}}$ are concerned, Dirichlet boundary conditions $\mathbf{u}_h(z_{\text{top}}) = \mathbf{u}_{\text{LS}}(z_{\text{top}})$ and $\phi(z_{\text{top}}) = \phi_{\text{LS}}(z_{\text{top}})$ are prescribed.

Model (1) is a first step before evolving toward a more advanced surrogate model including horizontal advection and fine-scale pressure gradient in the future. A particular focus of the present study is on the appropriate choice of a closure scheme to

175 diagnose the eddy diffusivities K_m and K_s. This is a key step to properly represent the downward mixing process.

2.3 Turbulence closure scheme

This subsection describes the turbulence scheme used to compute the eddy diffusivity for momentum and scalars. Those eddy diffusivities are responsible for a vertical mixing of atmospheric variables due to turbulent processes. The turbulence scheme we have implemented in our ABL1d model is very similar to the so-called CBR-1d scheme of Cuxart et al. (2000) which is

180 used operationally at Meteo France (Bazile et al., 2012). We chose to recode the parameterization from scratch for several reasons: computational efficiency, consistency with the NEMO coding rules, use of a geopotential vertical coordinate, and flexibility to add elements specific of the marine atmospheric boundary layer.

---

[2]Integrated Forecasting System: https://www.ecmwf.int/en/forecasts/documentation-and-support/changes-ecmwf-model/ifs-documentation
[3]http://aerobulk.sourceforge.net/

CBR-1d is a one-equation turbulence closure model based on a prognostic turbulent kinetic energy (TKE) and a diagnostic computation of appropriate length scales. The prognostic equation for the TKE $e = \frac{1}{2}\left(\langle u'u'\rangle + \langle v'v'\rangle + \langle w'w'\rangle\right)$ (with $\langle \cdot \rangle$ the Reynolds averaging operator) is

$$\partial_t e = -\langle \mathbf{u}'_h w' \rangle \cdot \partial_z \langle \mathbf{u}_h \rangle + \frac{g}{\theta_v^{\mathrm{ref}}} \langle w'\theta_v' \rangle - \partial_z \left(\langle e'w' \rangle + \frac{1}{\rho_a} \langle p'w' \rangle \right) - \varepsilon \tag{5}$$

where horizontal terms and vertical advection are neglected, as usually done in mesoscale atmospheric models. Here θ_v is the virtual potential temperature, ρ_a is atmospheric density, and ε a dissipation term. In order to express the evolution of e in terms of Reynolds averaged atmospheric variables, the following closure assumptions for the first order turbulent fluxes are made:

$$g \langle w'\theta_v' \rangle / \theta_v^{\mathrm{ref}} = -K_s N^2,$$

$$-\langle \mathbf{u}'_h w' \rangle \cdot \partial_z \langle \mathbf{u}_h \rangle = K_m \left[(\partial_z \langle u \rangle)^2 + (\partial_z \langle v \rangle)^2 \right]$$

$$-\left(\rho_a^{-1} \partial_z \langle w'p' \rangle + \partial_z \langle w'e' \rangle \right) = K_e \partial_z e$$

$$\varepsilon = c_\varepsilon e^{3/2}/l_\varepsilon$$

where l_ε is a dissipative length scale, c_ϵ a constant, and N^2 is the moist Brunt-Väisälä frequency computed as $N^2 = (g/\theta_v^{\mathrm{ref}})(\partial_z \langle \theta \rangle + 0.608\, \partial_z(\langle \theta \rangle \langle q \rangle))$ with $\theta_v^{\mathrm{ref}} = 288$ K. Under those hypothesis the TKE prognostic equation is

$$\partial_t e = K_m \|\partial_z \langle \mathbf{u}_h \rangle\|^2 - K_s N^2 + \partial_z (K_e \partial_z e) - \frac{c_\varepsilon}{l_\varepsilon} e^{3/2} \tag{6}$$

The eddy diffusivities for momentum K_m, TKE K_e and scalars K_s all depend on e and on a mixing length scale l_m

$$(K_m, K_s, K_e) = (C_m, C_s \phi_z, C_e) l_m \sqrt{e}$$

with (C_m, C_s, C_e) a triplet of constants and ϕ_z a stability function proportional to the inverse of a turbulent Prandtl number, given by

$$\phi_z(z) = \left(1 + \max\left\{ C_1 l_m l_\varepsilon N^2/e, -0.5455 \right\}\right)^{-1}.$$

The ϕ_z function is bounded not to exceed $\phi_z^{\mathrm{max}} = 2.2$ as done in the Arpege model of Meteo-France (e.g. Bazile et al., 2012). Assuming that the minimum of ϕ_z is attained in the linearly stratified limit (i.e. for $l_m = l_\varepsilon = \sqrt{2e/N^2}$), values of the maximum Prandtl number $\mathrm{Pr}_t = C_m/(C_s\phi_z)$ are given in Tab. 1. Constant values for $C_m, C_s, C_e, c_\varepsilon$, and C_1 can be determined from different methods, leading to nearly similar values. The traditional way is to use the inertial-convective subrange theory of locally isotropic turbulence (Lilly, 1967; Deardorff, 1974). Another way relies on a theoretical turbulence model partly based on renormalization group methods (see Cheng et al., 2002). For the present study, the sets proposed by Cuxart et al. (2000) and Cheng et al. (2002) will be considered (Tab. 1). A major difference between the two sets concerns the value of C_m. This difference is explained by a reevaluation of the energy redistribution among velocity components by pressure fluctuations, whose magnitude is assumed to be proportional to the degree of energy anisotropy as initially introduced by Rotta (1951). Note that the constant set of Cheng et al. (2002) is now used by default in both research and operational Meteo-France models.

	C_m	C_s	C_e	c_ε	C_1	$\mathrm{Pr}_\mathrm{t}^{\min}$	$\mathrm{Pr}_\mathrm{t}^{\max}$	$l_m^{\min}$
Cuxart et al. (2000) (CBR00)	0.0667	0.1667	0.4	0.7	0.139	0.182	0.511	1.5m
Cheng et al. (2002) (CCH02)	0.126	0.143	0.34	0.845	0.143	0.182	0.515	0.79m

Table 1. Set of turbulence scheme constants from Cuxart et al. (2000) and Cheng et al. (2002). $\mathrm{Pr}_\mathrm{t} = C_m/(C_s\phi_z)$ is the turbulent Prandtl number.

Dirichlet boundary conditions for TKE are applied at the top $z = z_\mathrm{top}$ and at the bottom $z = z_\mathrm{sfc}$

$$
\begin{aligned}
e(z = z_\mathrm{sfc}) &= e_\mathrm{sfc} = \frac{u_\star^2}{\sqrt{C_m c_\varepsilon}} + 0.2 w_\star^2 \\
e(z = z_\mathrm{top}) &= e_\mathrm{min} = 10^{-6} \ \mathrm{m}^2 \, \mathrm{s}^{-2}
\end{aligned}
\tag{7}
$$

215 with $u_\star$ and $w_\star$ the friction and convective velocities given by the bulk formulation. The value for e_min has been chosen empirically as well as background values $K_m^{\min} = 10^{-4} \ \mathrm{m}^2 \, \mathrm{s}^{-1}$ and $K_s^{\min} = 10^{-5} \ \mathrm{m}^2 \, \mathrm{s}^{-1}$ for eddy diffusivities. The value of e_sfc arise from the similarity theory in the surface layer under the assumption of an equilibrium between TKE shear production, buoyancy production/destruction, and dissipation (Redelsperger et al., 2001). The minimum value for l_m is simply set as $l_m^{\min} = \frac{K_m^{\min}}{C_m \sqrt{e_\mathrm{min}}}$. There are multiple options to compute the mixing lengths l_m and l_ε (this point will be discussed later in Sec.

220 3.2) but all options have identical boundary conditions

$$
l_m(z = z_\mathrm{sfc}) = L_\mathrm{sfc} = \kappa \frac{(C_m c_\varepsilon)^{1/4}}{C_m}(z_\mathrm{sfc} + z_0), \qquad l_m(z = z_\mathrm{top}) = l_m^{\min}
\tag{8}
$$

Again the value of L_sfc results from the similarity theory in the neutrally stratified surface layer (Sec. 4.1 in Redelsperger et al., 2001). In (8), κ is the von Karman constant and z_0 a roughness length computed within the bulk algorithm.

Our current implementation of boundary layer subgrid processes is an eddy-diffusivity approach which does not include any
225 explicit representation of boundary-layer convective structures. This could be done via a mass-flux representation (e.g. Hourdin et al., 2002; Soares et al., 2004) or the introduction of a countergradient term (e.g. Troen and Mahrt, 1986). This point is left for future developments of the ABL1d model.

2.4 Processing of large-scale forcing and Newtonian relaxation

As mentioned earlier, the ABL1d model (1) requires three-dimensional (x, y, z) large-scale atmospheric variables $\phi_\mathrm{LS}^\mathrm{atm}$ while
230 existing uncoupled oceanic forcing strategies require only two-dimensional (x, y) atmospheric variables. This is a difficulty for efficiency reasons since it substantially increases the number of I/Os but also for practical reasons because it requires the development of a dedicated tool to extract large-scale atmospheric data and interpolate them on prescribed geopotential heights from their native vertical grid which can be either pressure based or arbitrary Lagrangian Eulerian. Such tools have been developed specifically to work with ERA-Interim, ERA5 and operational IFS datasets and are described in App. A.

235 Beyond the particular values of $\phi_\mathrm{LS}^\mathrm{atm}$, the form of the relaxation timescale has great impact on model solutions. The vertical profile for the λ_m and λ_s coefficients in (1) is chosen to nudge strongly above the MABL and moderately in the MABL with

a smooth transition between its minimum and maximum value to avoid large vertical gradients in λ_m and λ_s which would result in artificially large vertical gradients in atmospheric variables. In practice the $\lambda_m(z)$ and $\lambda_s(z)$ functions depend on the following parameters

240    $(\lambda_m^{\max}, \lambda_m^{\min})$ and $(\lambda_s^{\max}, \lambda_s^{\min})$ which define the maximum and minimum of the nudging coefficient respectively for momentum and scalars. Following equation (2), a guideline to set reasonable values for those parameter values would be to make sure that $\Delta t \lambda_s^{\max} \approx 1$ (i.e. the large scale value is imposed above the boundary layer), and $\Delta t \lambda_s^{\min} \approx 1/10$ (i.e. the boundary layer values are the result of a weighting with a weight 0.9 for the ABL1d prediction and 0.1 for the large scale value).

245    $(\beta_{\min}, \beta_{\max})$ which define the extent of the transition zone separating the maximum and minimum of the nudging coefficient

We considered the following general form for $\lambda_s(z)$ (resp. $\lambda_m(z)$), with h_{bl} the boundary layer height whose value is diagnosed using an integral Richardson number criteria (Sec. 3.2 and 3.3 in Lemarié et al., 2012) with a critical value equal to C_1 :

$$
\lambda_s(z) = \begin{cases} \lambda_s^{\min}, & z \leq \beta_{\min} h_{\mathrm{bl}} \\ \sum_{m=0}^{3} \alpha_m \left(\dfrac{z}{h_{\mathrm{bl}}} \right)^m, & z \in]\beta_{\min} h_{\mathrm{bl}}; \beta_{\max} h_{\mathrm{bl}}[\\ \lambda_s^{\max}, & z \geq \beta_{\max} h_{\mathrm{bl}} \end{cases} \tag{9}
$$

250   where four α_m coefficients are necessary to guarantee the continuity of $\lambda_s(z)$ and its derivative $\partial_z \lambda_s$ at $z = \beta_{\min} h_{\mathrm{bl}}$ and $z = \beta_{\max} h_{\mathrm{bl}}$. We easily find

$$
\alpha_0 = \frac{(3\beta_{\max} - \beta_{\min})\beta_{\min}^2 \lambda_s^{\max} + (\beta_{\max} - 3\beta_{\min})\beta_{\max}^2 \lambda_s^{\min}}{(\beta_{\max} - \beta_{\min})^3}, \qquad \alpha_1 = -\frac{6\beta_{\max}\beta_{\min}(\lambda_s^{\max} - \lambda_s^{\min})}{(\beta_{\max} - \beta_{\min})^3}
$$

$$
\alpha_2 = 3\frac{(\beta_{\max} + \beta_{\min})(\lambda_s^{\max} - \lambda_s^{\min})}{(\beta_{\max} - \beta_{\min})^3}, \qquad \alpha_3 = -\frac{2(\lambda_s^{\max} - \lambda_s^{\min})}{(\beta_{\max} - \beta_{\min})^3}
$$

The value of h_{bl} is bounded beforehand to guarantee that at least 3 grid points are such that $z \leq \beta_{\min} h_{\mathrm{bl}}$ and $z \geq \beta_{\max} h_{\mathrm{bl}}$. A typical profile of the $\lambda_s(z)$ is shown in Fig. 1a.

255   When the model is forced by the large-scale pressure gradient (or the geostrophic winds), the parameter $\lambda_m(z)$ should be theoretically zero at high and mid latitudes. However for the equatorial region, a Newtonian relaxation toward the large scale winds should be maintained. To do so, the coefficient $\lambda_m(z)$ is multiplied by a coefficient r_{eq} which is a function of the Coriolis parameter f. The r_{eq} coefficient equal to zero for large values of $|f|$ and increases to one when approaching the equator. The following form satisfies those constraints (see also Fig. 1b)

260    $$
r_{\mathrm{eq}}(f) = \sin\left(\frac{\pi}{2} \left[\frac{f - f_{\max}}{f_{\max}} \right] \right)^6, \qquad f_{\max} = \frac{2\pi}{12 \times 3600} \, \mathrm{s}^{-1}. \tag{10}
$$

3 Numerical discretization and implementation within NEMO

The formulation (1) of the ABL1d model is discretized in time with an Euler backward scheme for the vertical diffusion terms, semi-implicitly for the Coriolis term and explicitly for the relaxation term which means that the model is stable as long as

Figure 1. a) Typical profile of the nudging coefficient $\lambda_s(z)$ with respect to the parameters $\lambda_s^{\max}, \lambda_s^{\min}, \beta_{\min}, \beta_{\max}, h_{\rm bl}$. b) Equatorial restoring function $r_{\rm eq}$ with respect to the Coriolis frequency f.

$$\varphi = e, l_m, l_\varepsilon, N^2, K_m, K_s, K_e$$
$$\phi = u, v, \theta, q, \lambda_m, \lambda_s$$
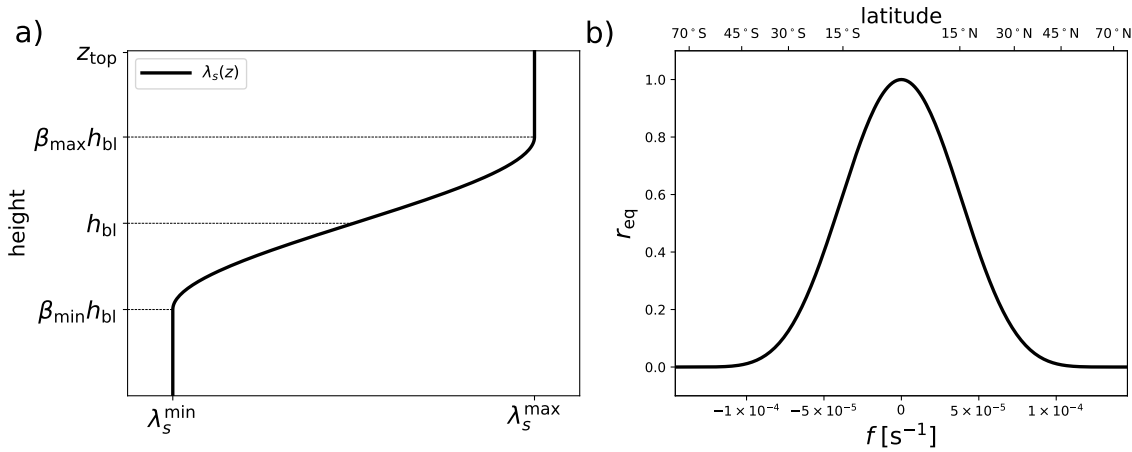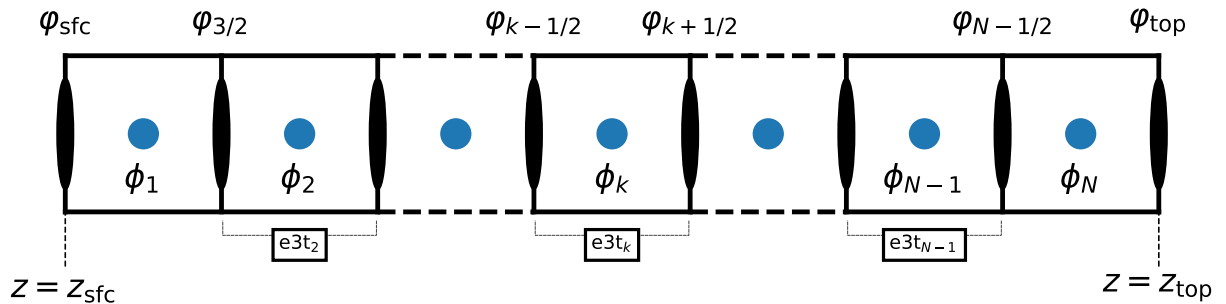
Figure 2. Vertical grid variable arrangements and important notations.

$\lambda_s \Delta t \leq 1$. The variables are defined on a non-staggered grid in the horizontal (a.k.a Arakawa A-grid). Because we consider a
265 computational domain exclusively over water or sea-ice, topography is not considered and vertical levels are flat and fixed in time which, among other things, allows to interpolate the large-scale data $\phi_{\rm LS}$ on the vertical grid offline. The position of the various quantities introduced so far on the computational grid is given in Fig. 2. In this section we provide additional details on the discretization of the Coriolis term, TKE equation, mixing lengths, and of the boundary conditions at $z = z_{\rm sfc}$.

3.1 Coriolis term treatment

270 Since in our implementation the horizontal velocity components are collocated, the discretization of the Coriolis term is straightforward and is energetically neutral. In the event the ABL1d is integrated with a time-step much larger than the oceanic time-step, a specific care must be given to the stability of the Coriolis term time-stepping. For a given grid cell with index (i,j), a semi-implicit scheme with weighting parameter γ reads

$$
\begin{aligned}
u_{i,j}^{n+1,\star} &= u_{i,j}^n + (f\Delta t)\left((1-\gamma)v_{i,j}^n + \gamma v_{i,j}^{n+1,\star}\right) \\
v_{i,j}^{n+1,\star} &= v_{i,j}^n - (f\Delta t)\left((1-\gamma)u_{i,j}^n + \gamma u_{i,j}^{n+1,\star}\right)
\end{aligned}
\tag{11}
$$

275 The exponent $\star$ is used here to emphasize that $u_{i,j}^{n+1,\star}$ and $v_{i,j}^{n+1,\star}$ are temporary values at time $n+1$ before vertical diffusion and Newtonian relaxation are applied. (11) can be written in a more compact way as

$$
\begin{aligned}
u_{i,j}^{n+1,\star} &= \frac{(1-\gamma(1-\gamma)(f\Delta t)^2)u^n + (f\Delta t)v^n}{1+(f\Delta t)^2\gamma^2} \\
v_{i,j}^{n+1,\star} &= \frac{(1-\gamma(1-\gamma)(f\Delta t)^2)v^n - (f\Delta t)u^n}{1+(f\Delta t)^2\gamma^2}.
\end{aligned}
$$

The associated amplification factor modulus is $|\mathcal{A}_{\mathrm{cor}}| = \sqrt{\dfrac{1+(1-\gamma)^2(f\Delta t)^2}{1+\gamma^2(f\Delta t)^2}}$ meaning that unconditional stability is ob-

280 tained as long as $\gamma \geq 1/2$. For the numerical results obtained below in Sec. 4 and 5 we used $\gamma = 0.55$ which is deliberately slightly dissipative.

3.2 TKE positivity-preservation and mixing lengths computation

In Sec. 2.3 we have presented the continuous formulation of the TKE-based turbulence closure of the ABL1d model. The TKE equation is discretized using a backward Euler scheme in time with a linearization of the dissipation term $\dfrac{c_\varepsilon}{l_\varepsilon}e^{3/2}$ which

285 is discretized as $\dfrac{c_\varepsilon}{l_\varepsilon}\sqrt{e^n}e^{n+1}$. However, such discretization is not unconditionally positivity-preserving for TKE which could give rise to unphysical solutions (e.g. Burchard, 2002b). Ignoring the diffusion term, the TKE prognostic equation (6) can be written as an ordinary differential equation (ODE) of the form

$$
\partial_t e = S(\mathbf{u}_h, N^2) - D(e,t)\,e, \qquad \text{with } S(\mathbf{u}_h,N^2) = K_m\|\partial_z\mathbf{u}_h\|^2 - K_t N^2,\ D(e,t) = \frac{c_\varepsilon}{l_\varepsilon}\sqrt{e^n}
\tag{12}
$$

where the last term can be seen as a damping term. For ODEs like (12) it can be shown that for an initial condition $e(0) \geq 0$ and

290 $S(\mathbf{u}_h, N^2) \geq 0$, the solution $e(t)$ keeps the same sign as $e(0)$ whatever the sign of the damping coefficient $D(e,t)$. Assuming that $S(\mathbf{u}_h,N^2)$ and $D(e,t)$ are positive, a backward Euler discretization of the damping term in (12) would lead to

$$
e^{n+1} = \frac{e^n + \Delta t S(\mathbf{u}_h,N^2)}{1+\Delta t D(e,t)}
$$

which preserves positivity since for $e^n \geq 0$ we obtain $e^{n+1} \geq 0$. However, there is no guarantee that the forcing term $S(\mathbf{u}_h,N^2)$ is positive in particular when the shear is weak and the stratification is large. When $S(\mathbf{u}_h,N^2)$ is negative a specific treatment

295 (known as "Patankar trick", see Deleersnijder et al., 1997; Burchard, 2002b) is required. In the event of a negative $S(\mathbf{u}_h, N^2)$, the idea is to move the buoyancy term from S to D after dividing it by e^n, such that $S(\mathbf{u}_h, N^2) = K_m \|\partial_z \mathbf{u}_h\|^2$ is now strictly positive and $D(e, t) = \dfrac{c_\varepsilon}{l_\varepsilon}\sqrt{e^n} + K_s \dfrac{N^2}{e^n}$. Such procedure is a sufficient condition to preserve the positivity of the TKE without ad-hoc clipping of negative values. Moreover our discretization of the shear and buoyancy terms in the TKE equation is done in an energetically-consistent way following Burchard (2002a).

300 An other challenging task when implementing a TKE scheme is the discretization of the mixing lengths. As mentioned earlier, 4 different discretizations of l_m (resp. l_ε) have been coded. All discretizations consider the boundary conditions given in (8). The values of l_m and l_ε are traditionally computed from two intermediate length scales l_up and l_dwn which respectively correspond to the maximum upward and downward displacement of a parcel of air with a given initial kinetic energy. Once l_up and l_dwn have been estimated by one of the method described below, the dissipative and mixing length scale l_m and l_ε are

305 computed as

$$l_\mathrm{m} = \left(\frac{1}{2}\left\{ l_\mathrm{up}^{\frac{1}{a}} + l_\mathrm{dwn}^{\frac{1}{a}} \right\} \right)^a, \qquad \text{with } a = -\left(\frac{\log(c_\varepsilon) - 3\log(C_m) + 4\log(\kappa)}{\log 16} \right) \tag{13}$$

$$l_\varepsilon = \min\left(l_\mathrm{up}, l_\mathrm{dwn} \right) \tag{14}$$

where $a \approx -\frac{3}{2}$ for CBR00 and $a \approx -\frac{\sqrt{3}}{2}$ for CCH02. The impact of the weighting between l_up and l_dwn to compute l_m can be significant for idealized experiments like the ones presented in Sec. 4.1 but for more realistic cases results are weakly sensitive

310 and equivalent to the ones obtained with the simpler weighting $l_m = \sqrt{l_\mathrm{up} l_\mathrm{dwn}}$.

3.2.1 Bougeault and Lacarrère (1989) length scale

A classical approach in atmospheric models is the use of the Bougeault and Lacarrère (1989) mixing length which defines l_up and l_dwn as

$$\int\limits_z^{z+l_\mathrm{up}} N^2(s)(s-z)ds = e(z), \qquad \int\limits_{z-l_\mathrm{dwn}}^z N^2(s)(z-s)ds = e(z). \tag{15}$$

315 By construction such mixing lengths are bounded by the distance to the bottom and the top of the computational domain. It is worth noting that for $N^2 = \mathrm{cste}$, (15) gives respectively $\dfrac{l_\mathrm{up}^2 N^2}{2} = e(z)$ and $\dfrac{l_\mathrm{dwn}^2 N^2}{2} = e(z)$ which is equivalent to the Deardorff (1980) length scale. An objective is to satisfy this property also at a discrete level. Considering a simple trapezoidal rule to approximate the integral in (15) over each grid cells, the procedure for the computation of $l_\mathrm{up}(z_{k+1/2})$ is given in Algorithm 1. In the case $N^2(z_{p+1/2}) = N^2(z_{p-1/2}) = N_\mathrm{cst}^2 \ (\forall p)$, Algorithm 1 gives the following sequence

320
$$\mathrm{FC}(z_{k+1/2}) = -e(z_{k+1/2})$$
$$\mathrm{FC}(z_{k+3/2}) = -e(z_{k+1/2}) + N_\mathrm{cst}^2 \frac{\mathrm{e3t}(z_{k+1})^2}{2}$$
$$\mathrm{FC}(z_{k+5/2}) = -e(z_{k+1/2}) + N_\mathrm{cst}^2 \frac{[\mathrm{e3t}(z_{k+1}) + \mathrm{e3t}(z_{k+2})]^2}{2}$$
$$\cdots \qquad \cdots$$

Algorithm 1 Procedure to compute the Bougeault and Lacarrère (1989) length scale $l_{\mathrm{up}}(z_{k+1/2})$.

Initialize FC : $\mathrm{FC}(z_{k+1/2}) = -e(z_{k+1/2})$

for $p = k+1, N$ **do**

$\quad \mathrm{FC}(z_{p+1/2}) = \mathrm{FC}(z_{p-1/2}) + \dfrac{\mathrm{e3t}(z_p)}{2}\left(N^2(z_{p+1/2})(z_{p+1/2}-z_{k+1/2}) + N^2(z_{p-1/2})(z_{p-1/2}-z_{k+1/2})\right)$

$\quad$**if** $\mathrm{FC}(z_{p+1/2}) \times \mathrm{FC}(z_{p-1/2}) \leq 0$ **then**

$\quad\quad z_{k+1/2} + l_{\mathrm{up}} \in [z_{p-1/2}, z_{p+1/2}]$

$\quad\quad$**break**

$\quad$**end if**

end for

Linearly interpolate FC between $z_{p-1/2}$ and $z_{p+1/2}$ to find $z_\star$ such that $\mathrm{FC}(z_\star) = 0$.

As soon as $\mathrm{FC}(z_{p+1/2})$ changes sign we stop the procedure because l_{up} such that $-e(z_{k+1/2}) + N_{\mathrm{cst}}^2 l_{\mathrm{up}}^2 = 0$, which corresponds
325 to the Deardorff (1980) length scale, has been found. In the remainder we will note l_{BL89} the mixing length corresponding to
the Bougeault and Lacarrère (1989) algorithm.

3.2.2 Adaptation of NEMO's length scale

The standard NEMO algorithm (Sec. 10.1.3 in Madec, 2012) is a simpler and more efficient version of the Bougeault and
Lacarrère (1989) which is much easier to discretize. As a first step the Deardorff (1980) length scale l_{D80} is computed at cell
330 interfaces, such that

$$(l_{\mathrm{D80}})_{k+1/2} = \max\left(\sqrt{\frac{2e_{k+1/2}}{\max\left(N^2, N_\varepsilon^2\right)}}, l_{\min}\right)$$

with N_ε^2 the minimum stratification allowed whose value is set to the smallest positive real computer value. The vertical
gradients of l_{D80} are then limited such that they stay smaller than the variations of height. This amounts to compute l_{up} and
l_{dwn} as

335 $$(l_{\mathrm{up}})_{k-1/2} \quad = \quad \min\left((l_{\mathrm{up}})_{k+1/2} + \mathrm{e3t}_k, (l_{\mathrm{D80}})_{k-1/2}\right) \tag{16}$$

$$(l_{\mathrm{dwn}})_{k+1/2} \quad = \quad \min\left((l_{\mathrm{dwn}})_{k-1/2} + \mathrm{e3t}_k, (l_{\mathrm{D80}})_{k+1/2}\right) \tag{17}$$

with $\mathrm{e3t}_k$ the thickness of vertical layer k (Fig. 2). The resulting mixing length will be simply referred to as l_{D80}. Note that the
Taylor expansion of the integral in the Bougeault and Lacarrère (1989) mixing length definition is

$$\int\limits_z^{z+l_{\mathrm{up}}} N^2(s)(s-z)ds \approx \frac{N^2(z)l_{\mathrm{up}}^2}{2} + \frac{\frac{dN^2}{dz}l_{\mathrm{up}}^3}{3} + \mathcal{O}(l_{\mathrm{up}}^4),$$

340 which shows that the l_{D80} mixing length is an approximation of l_{BL89} which is obtained by retaining only the leading order
term in the Taylor expansion.

3.2.3   Rodier et al. (2017) length scale

Recently, Rodier et al. (2017) proposed a modification of the Bougeault and Lacarrère (1989). This modification turns out to improve results for stably stratified boundary layers typical of areas covered by ice. They propose to add a shear related term

345   to (15) such that the definition of l_{up} and l_{dwn} becomes

$$\int\limits_{z}^{z+l_{\mathrm{up}}} \left[N^2(s)(s-z) + c_0\sqrt{e(s)}\|\partial_s \mathbf{u}_h\| \right] ds = e(z), \qquad \int\limits_{z-l_{\mathrm{dwn}}}^{z} \left[N^2(s)(z-s) + c_0\sqrt{e(s)}\|\partial_s \mathbf{u}_h\| \right] ds = e(z). \qquad (18)$$

where c_0 is a parameter whose value should be smaller than $\sqrt{C_m/c_\varepsilon}$. The value of c_0 will be chosen based on numerical experiments presented in Sec. 4. At a discrete level, the FC function in Algorithm 1 is replaced by

$$\mathrm{FC}(z_{p+1/2}) = \mathrm{FC}(z_{p-1/2}) \quad + \quad \frac{\mathrm{e3t}(z_p)}{2}\left(N^2(z_{p+1/2})(z_{p+1/2}-z_{k+1/2}) + N^2(z_{p-1/2})(z_{p-1/2}-z_{k+1/2}) \right)$$

350

$$+ \quad c_0\frac{\mathrm{e3t}(z_p)}{2}\left(\sqrt{e(z_{p+1/2})}\|\partial_z\mathbf{u}_h(z_{p+1/2})\| + \sqrt{e(z_{p-1/2})}\|\partial_z\mathbf{u}_h(z_{p-1/2})\| \right)$$

In the following this mixing length will be referred to as l_{R17}.

3.2.4   A local buoyancy and shear-based length scale

For the sake of computational efficiency, we have derived a local version of the Rodier et al. (2017) length scale which is original to the present paper. Under the assumption that l_{up} (resp. l_{dwn}) is small compared to the spatial variations of N^2, e,

355   and $\|\partial_z\mathbf{u}_h\|$, we end up with the following second-order equation for l_{up}

$$\frac{N^2(z)}{2}l_{\mathrm{up}}^2 + c_0\sqrt{e(z)}\|\partial_z\mathbf{u}_h\|l_{\mathrm{up}} = e(z)$$

whose unique positive solution is

$$l_{\mathrm{D80}}^\star(z) = \frac{2\sqrt{e(z)}}{c_0\|\partial_z\mathbf{u}_h\| + \sqrt{c_0^2\|\partial_z\mathbf{u}_h\|^2 + 2N^2(z)}}.$$

We easily find that $l_{\mathrm{D80}}^\star = l_{\mathrm{D80}}$ for $\|\partial_z\mathbf{u}_h\| = 0$, and $l_{\mathrm{D80}}^\star = \dfrac{\sqrt{e(z)}}{c_0\|\partial_z\mathbf{u}_h\|}$ for $N^2 = 0$ which is consistent with the shear based

360   length scale of Wilson and Venayagamoorthy (2015). Once $l_{\mathrm{D80}}^\star$ has been computed we apply the limitations (16) and (17) as in the NEMO algorithm.

The performance of those four length scales for various physical flows is discussed in Sec. 4.

3.3   Coupling with ocean and sea-ice

For the practical implementation of the ABL coupling strategy within a global oceanic model, a proper coupling method is

365   required for stability and consistency purposes (e.g. Lemarié et al., 2015; Beljaars et al., 2017; Renault et al., 2019a) and the ABL1d must have the ability to handle grid cells partially covered by sea-ice. For the coupling strategy, a so-called implicit flux

coupling which is unconditionally stable (App. B in Beljaars et al., 2017) and asymptotically consistent for $\Delta t \to 0$ (Renault et al., 2019a) is used. Because vertical diffusion in ABL1d is handled implicitly in time, the boundary conditions (3) should be provided at time $n+1$. The implicit flux coupling amounts to discretize the boundary conditions (3) as

$$K_m \partial_z \mathbf{u}_h|_{z=z_{\text{sfc}}}^{n+1} \quad = \quad C_D \|\mathbf{u}_h^n(z_{\text{sfc}}) - \widetilde{\mathbf{u}}_{\text{oce}}\|(\mathbf{u}_h^{n+1}(z_{\text{sfc}}) - \widetilde{\mathbf{u}}_{\text{oce}}) \tag{19}$$

$$K_s \partial_z \phi|_{z=z_{\text{sfc}}}^{n+1} \quad = \quad C_\phi \|\mathbf{u}_h^n(z_{\text{sfc}}) - \widetilde{\mathbf{u}}_{\text{oce}}\|(\phi^{n+1}(z_{\text{sfc}}) - \widetilde{\phi}_{\text{oce}}) \tag{20}$$

where $\widetilde{\mathbf{u}}_{\text{oce}}$ and $\widetilde{\phi}_{\text{oce}}$ are either the instantaneous values at time n if NEMO and ABL1d have the same time-step or an average over the successive oceanic substeps otherwise.

A particular care has also been given to the compatibility between the ABL1d model and SI^3 (Sea Ice model Integrated Initiative) the sea-ice component of NEMO. SI^3 is a multi-category model whose state variables relevant for our study are the ice surface temperature T_l^{ice} with associated fractional area a_l (for the lth category), and the ice velocity $\mathbf{u}^{\text{ice}}$ (same for all categories). Note that the values of the exchange coefficients over sea-ice C_D^{ice}, C_θ^{ice}, and C_q^{ice} are different from their oceanic counterparts but are the same over all sea-ice categories. At this point there are several strategies for the ABL1d/SI^3 coupling: (*i*) run the ABL1d model over each ice category l and then average atmospheric variables weighted by a_l, (*ii*) run a single ABL1d model with a category averaged surface flux. The second option has been preferred because it is much easier to implement and more computationally efficient. It amounts to consider an ice surface temperature averaged over all categories $T^{\text{ice}} = \sum_{l=1}^{n_{\text{cat}}} a_l T_l^{\text{ice}}$ for the computation of ice-atmosphere turbulent fluxes (T^{ice} also enters in the computation of q_{ice}). Noting F_{oce} the fraction of open water (lead), the boundary condition (19) and (20) are modified in

$$K_m \partial_z \mathbf{u}_h|_{z=z_{\text{sfc}}}^{n+1} \quad = \quad F_{\text{oce}} C_D \|\mathbf{u}_h^n(z_{\text{sfc}}) - \widetilde{\mathbf{u}}_{\text{oce}}\|(\mathbf{u}_h^{n+1}(z_{\text{sfc}}) - \widetilde{\mathbf{u}}_{\text{oce}}) + (1 - F_{\text{oce}}) C_D^{\text{ice}} \|\mathbf{u}_h^n(z_{\text{sfc}}) - \widetilde{\mathbf{u}}^{\text{ice}}\|(\mathbf{u}_h^{n+1}(z_{\text{sfc}}) - \widetilde{\mathbf{u}}^{\text{ice}})$$

$$K_s \partial_z \phi|_{z=z_{\text{sfc}}}^{n+1} \quad = \quad F_{\text{oce}} C_\phi \|\mathbf{u}_h^n(z_{\text{sfc}}) - \widetilde{\mathbf{u}}_{\text{oce}}\|(\phi^{n+1}(z_{\text{sfc}}) - \widetilde{\phi}_{\text{oce}}) + (1 - F_{\text{oce}}) C_\phi^{\text{ice}} \|\mathbf{u}_h^n(z_{\text{sfc}}) - \widetilde{\mathbf{u}}^{\text{ice}}\|(\phi^{n+1}(z_{\text{sfc}}) - \widetilde{\phi}^{\text{ice}})$$

Because the dynamics of sea-ice is computed before the thermodynamics (see Fig. 1 in Rousset et al., 2015), the ABL1d/SI^3 coupling follows the different steps

1. Compute surface fluxes over ice and ocean and integrate the ABL1d model for given values F_{oce}^n and a_l^n.

2. Compute the dynamics of sea-ice

3. Update F_{oce}^n and a_l^n in $F_{\text{oce}}^\star$ and $a_l^\star$ because of step 2.

4. Distribute the fluxes over each ice category considering the updated values $a_l^\star$ (Sec. 3.6 in Rousset et al., 2015)

5. Compute the thermo-dynamics of sea-ice

3.4 Additional details about the implementation

As described in Maisonnave and Masson (2015), the NEMO source code is organized to separate the ocean routines on one side and the routines responsible for the surface boundary conditions computation (including sea-ice and the coupling interfaces)
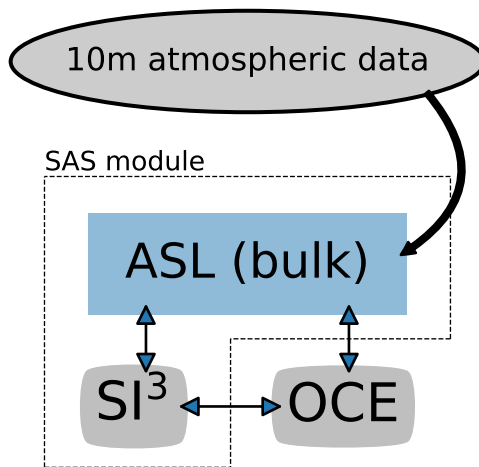
ASL forcing strategy   ABL coupling strategy
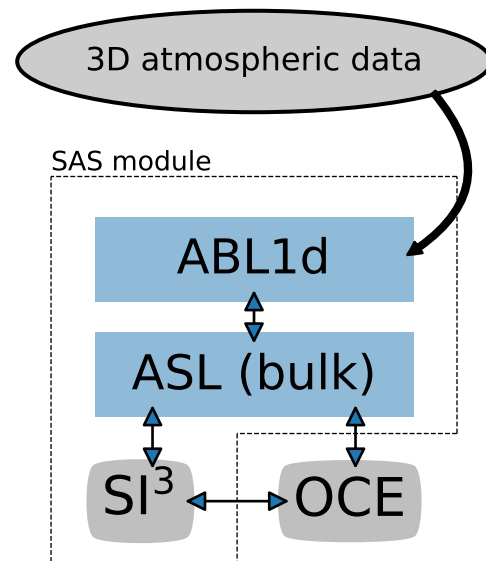
Figure 3. Schematic representation of the ASL forcing strategy (left) and ABL coupling strategy (right) in term of code organization and required external data. The OCE and SI^3 components represent respectively the oceanic and sea-ice dynamics and thermodynamics while the ASL component is in charge of providing boundary conditions related to atmospheric conditions. In the NEMO computational framework the so-called surface module (SAS component), delineated by dashed line polygons, is virtually separated from the OCE component which allows SAS to be run in standalone or detached mode (see Sec. 3.4).

on the other side. This makes a clear separation between the standard ocean model (OCE component) and the so-called surface module (SAS component). As schematically described in Fig. 3, the ABL1d model has been implemented within the SAS component which allows the following useful features

The ABL1d model can be run in standalone mode (coupled or not with sea-ice) with prescribed oceanic surface fields.

400   The ABL1d model can be run in detached mode, i.e. the OCE and SAS components run on potentially separate proces-
sors and computational grids communicating via the OASIS3 − MCT coupling library (Craig et al., 2017).

An other capability implemented within the NEMO modelling framework is the possibility to interpolate forcing fields on-the-fly. This is particularly useful for the ABL coupling strategy since three-dimensional atmospheric data must be interpolated on the ABL1d computational grid. As the current implementation of the on-the-fly interpolation only works in the horizontal, the
405   vertical interpolation of large-scale atmospheric data on the ABL1d vertical grid is done offline. Nevertheless it means that the size of input data compared to an ASL forcing strategy is N times larger with N the number of vertical levels in the ABL. A possibility to improve the efficiency for the reading of input data would be to take advantage of the parallel IO capabilities

	Units	Neutral case	GABLS1	SST front
Time-step	[s]	60	10	10
Simulation time	[h]	28	9	40
z_{top}	[m]	1500	400	2000
Vertical levels	-	40	64	50
Vertical resolution		uniform	uniform	stretched ($\Delta z \in [20, 100]$ m)
Coriolis parameter	[s^{-1}]	10^{-4}	1.39×10^{-4}	10^{-4}
Brunt-Väisälä frequency	[s^{-2}]	0	3.47×10^{-4}	10^{-4}
Geostrophic winds	[m s^{-1}]	$\mathbf{u}_G = (10,0)$	$\mathbf{u}_G = (8,0)$	$\mathbf{u}_G = (15,0)$
Roughness length	[m]	0.1	0.1	COARE3.0 bulk
Stability functions	-		$\begin{aligned} \psi_m &= -4.8(z/L_{\text{MO}}) \\ \psi_s &= -7.8(z/L_{\text{MO}}) \end{aligned}$	COARE3.0 bulk
θ_v^{ref}	[K]	-	283	288

Table 2. Description of the idealized experiments performed in Sec. 4. L_{MO} is the Monin-Obukhov length.

provided by the XIOS library (Xml-IO-Server, Meurdesoif et al., 2016) which is currently used in NEMO only for writing output data. This technical development is left for future work. This is a key aspect because, as discussed later in Sec. 5.3, the

410 main source of computational overhead associated with the ABL coupling strategy is due to the time spent waiting for input files to be read.

4 Atmosphere-only numerical experiments

To check the relevance of our ABL1d model for idealized atmospheric situations typical of the atmospheric boundary layer over water or sea-ice, we performed a set of single column experiments. Each of those experiments have been run with a companion

415 large-eddy simulation (LES) model whose solution is considered as the reference. In the following we consider a neutrally stratified and a stably stratified case as well as a case with a transition from stable to unstable stratification representative of an atmospheric flow over an SST front. All ABL1d simulations presented here have been performed directly within the SAS component of the NEMO modelling framework. Parameter values for each experiments are presented in Tab. 2. An objective of this section is to illustrate the type of sensitivity we can expect from the ABL1d model and discriminate between the various

420 options available in the code, i.e. choice of the set of coefficients (CBR00 vs CCH02), choice of l_m and l_ε among the algorithms described in Sec. 3.2.1-3.2.4 and choice of the appropriate value of c_0 in the l_{R17} and $l_{\text{D80}}^\star$ mixing length computation.

4.1 Neutral turbulent Ekman layer

We first propose to investigate the simulation of a neutrally stratified atmosphere analogous to a classical turbulent Ekman layer. The selected case is based on the setup described in Andren et al. (1994). The initial conditions for this experiment
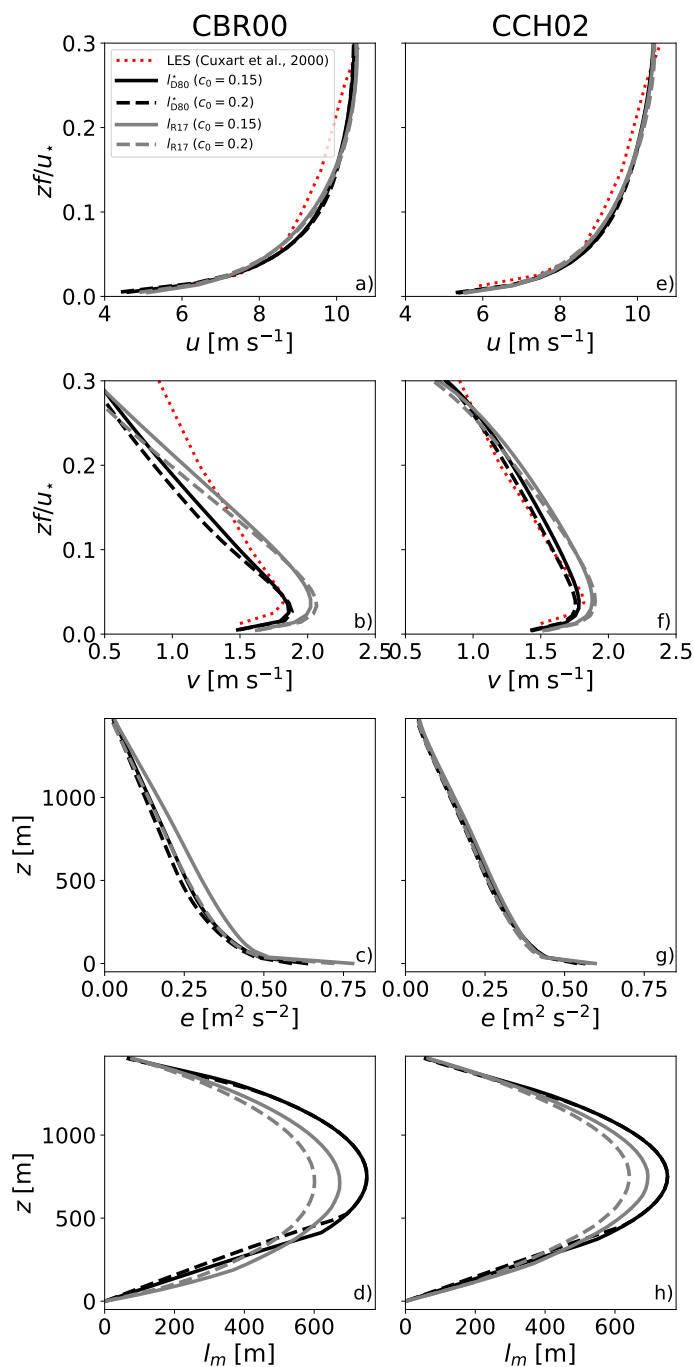
Figure 4. Results obtained for the neutral boundary-layer case of Andren et al. (1994) with the CBR00 model constants (left panels a to d) and CCH02 model constants (right panels d to e) for different parameter values for c_0 and different mixing length formulations ($l^\star_{D80}$ for black lines or l_{R17} for grey lines). Results are shown for u (panels a & e), v (panels b & f), e (panels c & g), and l_m (panels d & h). In the top four panels results are compared with LES simulations from Cuxart et al. (2000) (their Fig. 16). As in Andren et al. (1994), simulations were run over a period of $10/f$ and results are averaged over the last $3/f$ period.

425   are not defined analytically, they are given by Tab. A.1 in Andren et al. (1994)[4]. This testcase is mainly used to check the adequacy of our surface boundary conditions with similarity theory and the proper calibration of the parameter c_0 in the $l^{\star}_{\mathrm{D80}}$ and l_{R17} formulations of the mixing lengths. In theory, the l_{D80} and l_{BL89} mixing lengths do not support the asymptotic limit $N^2 = 0$ but for the integrity of numerical results a minimum threshold N^2_ε on the stratification is imposed in the code. In this case the procedure to compute those mixing lengths as described in Sec. 3.2.1 and 3.2.2 will provide identical results, namely

430    $l_{\mathrm{up}} = z_{\mathrm{top}} - z$ and $l_{\mathrm{dwn}} = z - z_{\mathrm{sfc}}$ (i.e. the distance from the top and from the bottom of the computational domain). We test here the $l^{\star}_{\mathrm{D80}}$ and l_{R17} introduced in Sec. 3.2. The reference solution is taken from Cuxart et al. (2000) (panels a) and b) in their Fig. 16). Results are obtained using the ABL1d model with either the CBR00 (Fig. 4, left panels) or the CCH02 (Fig. 4, right panels) set of parameters. All experiments have been done with $c_0 = 0.15$ and $c_0 = 0.2$. All simulations are able to reproduce the overall behaviour of the LES case. The best agreement is obtained when using the CCH02 model constants along with $l^{\star}_{\mathrm{D80}}$

435   mixing length formulation and $c_0 = 0.2$. The results obtained for l_{D80} and l_{BL89} are identical and close to the l_{R17} results with $c_0 = 0.15$ (not shown). Broadly speaking, all simulations with the CCH02 set of parameters show reasonable results.

4.2   Stably stratified boundary layer (GABLS1)

Within the Global Energy and Water Exchanges (GEWEX) Atmospheric Boundary Layer Study (GABLS), idealized cases for stable surface boundary layers have been investigated (e.g. Cuxart et al., 2006). Such conditions are typical of areas covered

440   with sea-ice. Here we consider the GABLS1 case whose technical description is available at http://turbulencia.uib.es/gabls/gabls1d_desc.pdf. This experiment is particularly interesting as significant differences generally exist between solutions obtained from LES and single-column simulations, for example when the Bougeault and Lacarrère (1989) length scale is used (e.g. Cuxart et al., 2006; Rodier et al., 2017). A large scale geostrophic wind is imposed as well as a cooling of the surface temperature $\theta_s(t)$ given by $\theta_s(t) = 263.5 - 0.25(t/3600\,\mathrm{s})$. The parameter values for this test are reported in Tab. 2 and the

445   initial conditions are $\mathbf{u}_h(z, t=0) = \mathbf{u}_G$, and

$$
\theta(z, t=0) = \left\{ \begin{array}{ll} 265 & z \leq 100\,\mathrm{m} \\ 265 + 0.01(z - 100) & \text{otherwise} \end{array} \right. , \qquad e(z, t=0) = \left\{ \begin{array}{ll} e_{\min} + 0.4(1 - z/250)^3 & z \leq 250\,\mathrm{m} \\ e_{\min} & \text{otherwise} \end{array} \right.
$$

The solutions after 9 hours of simulation are shown in Fig. 5 (left panels) for CBR00 parameter values and in Fig. 5 (right panels) for CCH02 parameter values. The reference solution is taken from Rodier et al. (2017) LES simulations. As expected, solutions based on a mixing length ignoring the contribution from the vertical shear exhibit a too thick boundary layer and

450   a wind speed maximum located too high in altitude. Using a buoyancy and shear based mixing length mitigates the issue and provides very good agreement with reference solutions when the CCH02 model constants are used. The best results are obtained for $l^{\star}_{\mathrm{D80}}$ with $c_0 = 0.2$ and l_{R17} with $c_0 = 0.15$. Solutions obtained with the CBR00 model constants systematically predict larger turbulent kinetic energy and mixing lengths resulting in large values of K_s in the first 100 meters near the surface

---

[4]However, we did not find significant differences in numerical solutions when using the following initial conditions :

$$
\mathbf{u}_h(z, t=0) = \mathbf{u}_G, \qquad e(z, t=0) = e_{\min}
$$
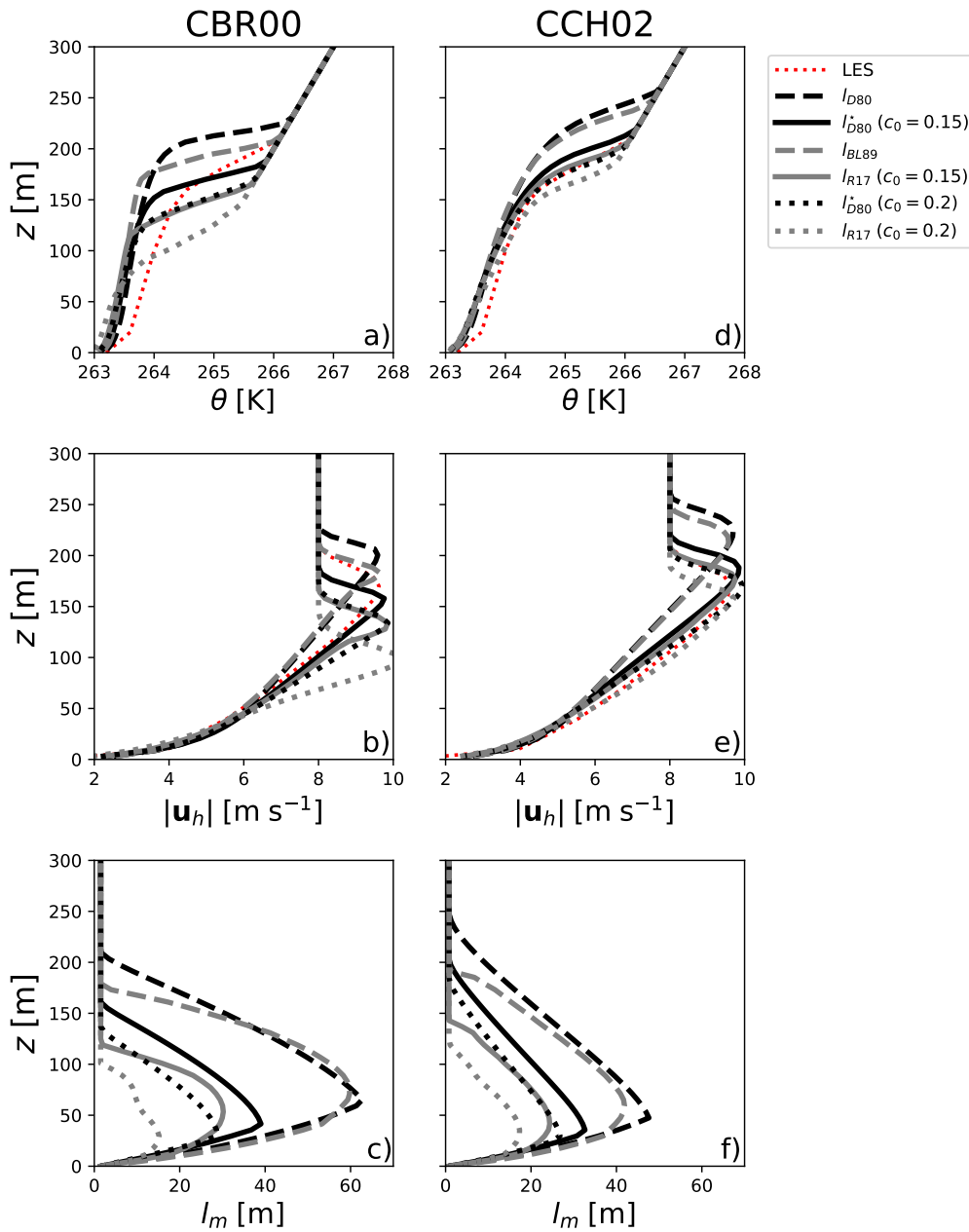
Figure 5. Results obtained for the stably stratified boundary-layer case of Cuxart et al. (2006) for the parameter values CBR00 (left panels a to c) and CCH02 (right panels d to f) with different mixing length formulations: l_{D80} for black solid lines, $l^{\star}_{D80}$ with $c_0 = 0.15$ for dashed black lines (resp. $c_0 = 0.2$ for dotted black lines), l_{BL89} for solid grey lines and l_{R17} with $c_0 = 0.15$ for dashed grey lines (resp. $c_0 = 0.2$ for dotted grey lines). Results are shown for potential temperature θ (panels a & d), wind speed (panels b & e), and l_m (panels c & f). Dotted red lines represent LES results from Rodier et al. (2017). Instantaneous profiles after 9 hours are shown.

(not shown). The mismatch in terms of TKE is partially explained by the difference in boundary condition since with CBR00
455   constants we have $e_{\mathrm{sfc}} = 4.628\, u_\star^2$ while with CCH02 constants we get $e_{\mathrm{sfc}} = 3.065\, u_\star^2$ from Eq. (7). Note that the proper
calibration of the c_0 constant jointly with the c_ε is the subject of several ongoing studies. Since our simulations reproduce the
known sensitivity to those parameters, the ABL1d model could directly benefit from new findings on that topic.

So far the CCH02 set of parameters turn out to provide results of better quality than the CBR00 constants. For the sake of
simplicity, we will retain only the CCH02 parameters for the numerical results shown in the remainder.

460   ### 4.3   Winds across a midlatitude SST front

4.3.1   Setup and reference solutions

An idealized experiment particularly relevant for the coupling of the MABL with mesoscale oceanic eddies (and potentially
submesoscale fronts) has been initially suggested by Spall (2007) and then revised by Kilpatrick et al. (2014). More recently
Ayet and Redelsperger (2019) derived an analytical model based on a similar setup. The geometry of the problem is two-
465   dimensional x-z with an SST front along the x-axis

$$\theta_s(x) = 288.95 + \frac{\Delta\theta}{2}\tanh\left(\frac{x}{L_\theta}\right)$$

where $\Delta\theta = 3\,\mathrm{K}$, $L_\theta = 100\,\mathrm{km}$, and $x \in [-1800\,\mathrm{km}, 1800\,\mathrm{km}]$. As indicated in Tab. 2, a zonal geostrophic wind of $15\,\mathrm{m\,s^{-1}}$
is prescribed balanced by a vertically homogeneous meridional pressure gradient. The wind thus flows over cold water before
reaching a warm SST anomaly 3 K warmer. We consider a dry case, the model is initialized $\forall x$ with

470   $$\theta(z, t=0) \quad = \quad 288.95 + \left(N^2 \theta^{\mathrm{ref}}/g\right) z$$
$$q(z, t=0) \quad = \quad 0$$

where $N^2 = 10^{-4}\,\mathrm{s^{-2}}$ and $\theta^{\mathrm{ref}} = 288\,\mathrm{K}$. The velocities are systematically initialized with geostrophic winds. All simulations
are run for 36 hours when the flow reaches a quasi-equilibrium state.

For this configuration the reference solution is obtained from the Mesoscale Non Hydrostatic model (MesoNH) v5.3.0
475   (Lafore et al., 1998; Lac et al., 2018) where microphysics and radiation packages have not been activated. The horizontal
resolution is $\Delta x = 1\,\mathrm{km}$ and the model is discretized with 91 vertical levels from the surface to 20 km height. The vertical
resolution near the surface is $\Delta z = 10\,\mathrm{m}$ and around $\Delta z = 100\,\mathrm{m}$ at 2000 m height. The turbulence scheme is the 1.5-order
closure of Cuxart et al. (2000) in its one-dimensional form with the l_{BL89} mixing length and CCH02 set of parameters. Sea
surface fluxes are computed using the bulk parameterisation COARE3.0. which is also available in NEMO from the Aerobulk
480   package. As far as the ABL1d model is concerned, the top of the computational domain is $z_{\mathrm{top}} = 2000\,\mathrm{m}$ and the vertical
grid is stretched with a typical resolution of 20 m near the surface and 100 m near $z = z_{\mathrm{top}}$ with a first grid point located at
$z = 10\,\mathrm{m}$. In the horizontal, the resolution is $\Delta x = 6\,\mathrm{km}$.
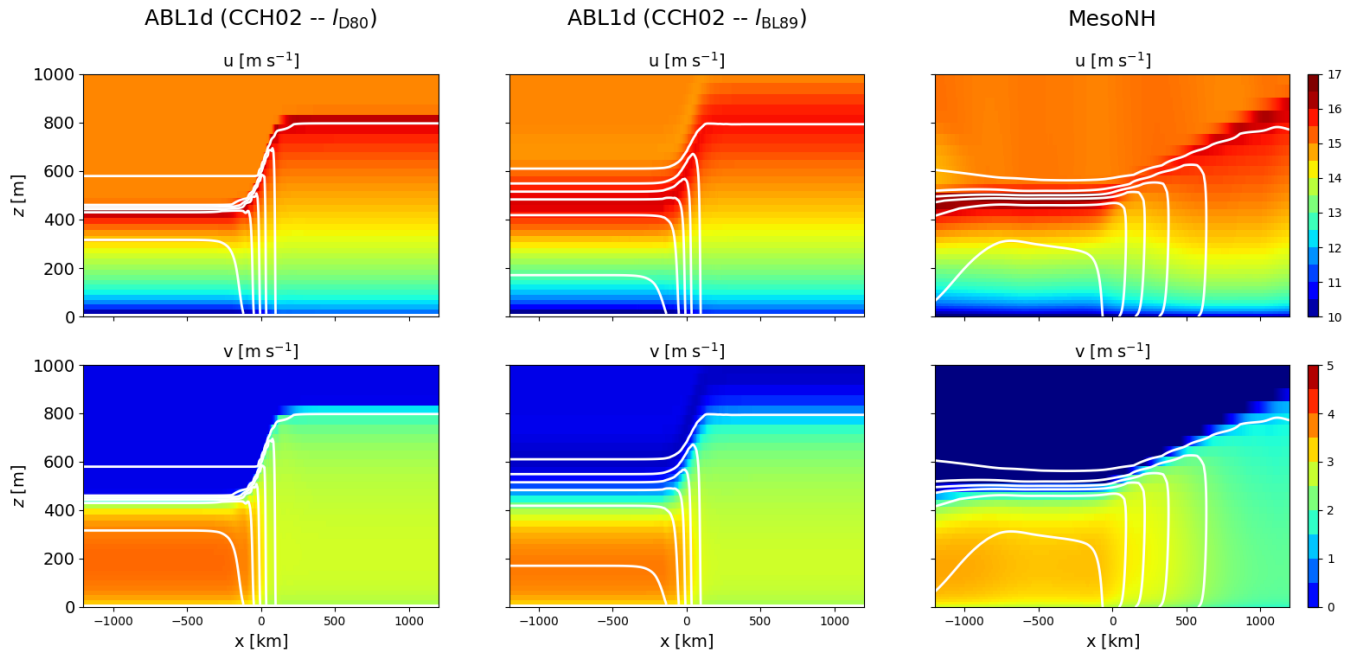
Figure 6. Zonal (top panels) and meridional (bottom panels) components of atmospheric winds for the reference MesoNH simulation (right panels) and for ABL1d simulations with l_{D80} mixing length and CCH02 model constants (left panels) and with l_{BL89} mixing length and CCH02 model constants (middle panels). Temperature contours are shown in white with a contour every $0.5°C$ between $15°C$ and $17.5°C$. The SST front is centered at $x = 0$ km.

4.3.2 Numerical results

For this configuration, results will be mostly evaluated in terms of 10 m winds $\mathbf{u}_{10}$ and temperature θ_{10}. As an illustration of the type of result we get, we first compare the MesoNH solution and the ABL1d solution obtained with the l_{D80} and l_{BL89} mixing-lengths in Fig. 6. It is worth noting that the MesoNH solution closely compares with the solution of Kilpatrick et al. (2014) (their Fig. 2) with a shallow boundary layer height (around 400 m) before the front and a thicker one (around 800 m) after the front where momentum mixing is enhanced. Over the front, as noted by Ayet and Redelsperger (2019) with similar setup, the effect of advection is predominant for meridional winds thus explaining the differences seen with the ABL1d simulations. Indeed with ABL1d, whatever the numerical options, the atmospheric column will locally adjust to the underlying oceanic conditions since horizontal advection is neglected. This explains the absence of horizontal lag when passing over the front in the ABL1d solution compared to the MesoNH solution. However, away from the SST front the solutions are very similar in terms of boundary layer height and vertical wind structure. In anticipation of a coupling with an oceanic model, the most important quantities to look at are the 10m atmospheric variables rather than the full 3D vertical structure of the MABL. In Fig. 7, the 10m wind components and temperature when the ABL1d model reaches a quasi-equilibrium state are shown for different mixing lengths options, as well as the MesoNH results. First the results obtained with the l_{R17} are very different from
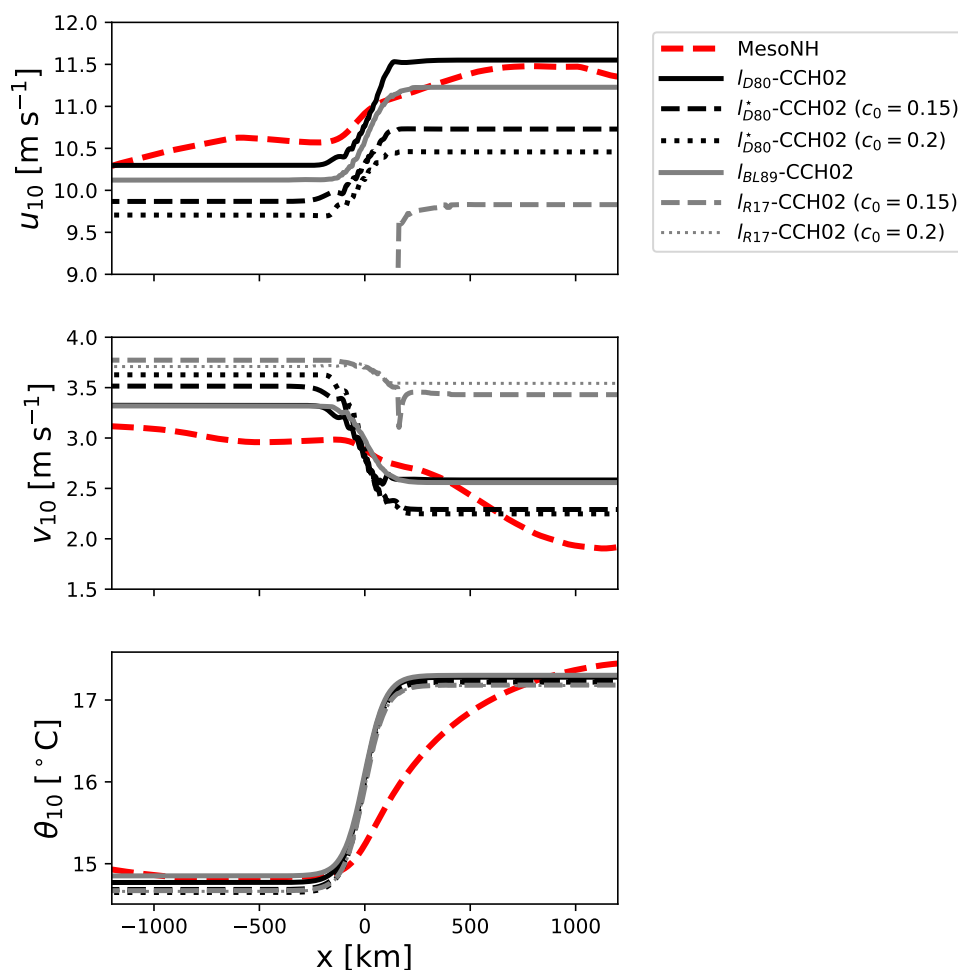
Figure 7. Zonal (top) and meridional (middle) components of $10\,\mathrm{m}$ winds and $10\,\mathrm{m}$ temperature (bottom) for the reference MesoNH simulation (dashed red) and for ABL1d simulations with different mixing lengths formulations for the winds across a midlatitude SST front experiment.
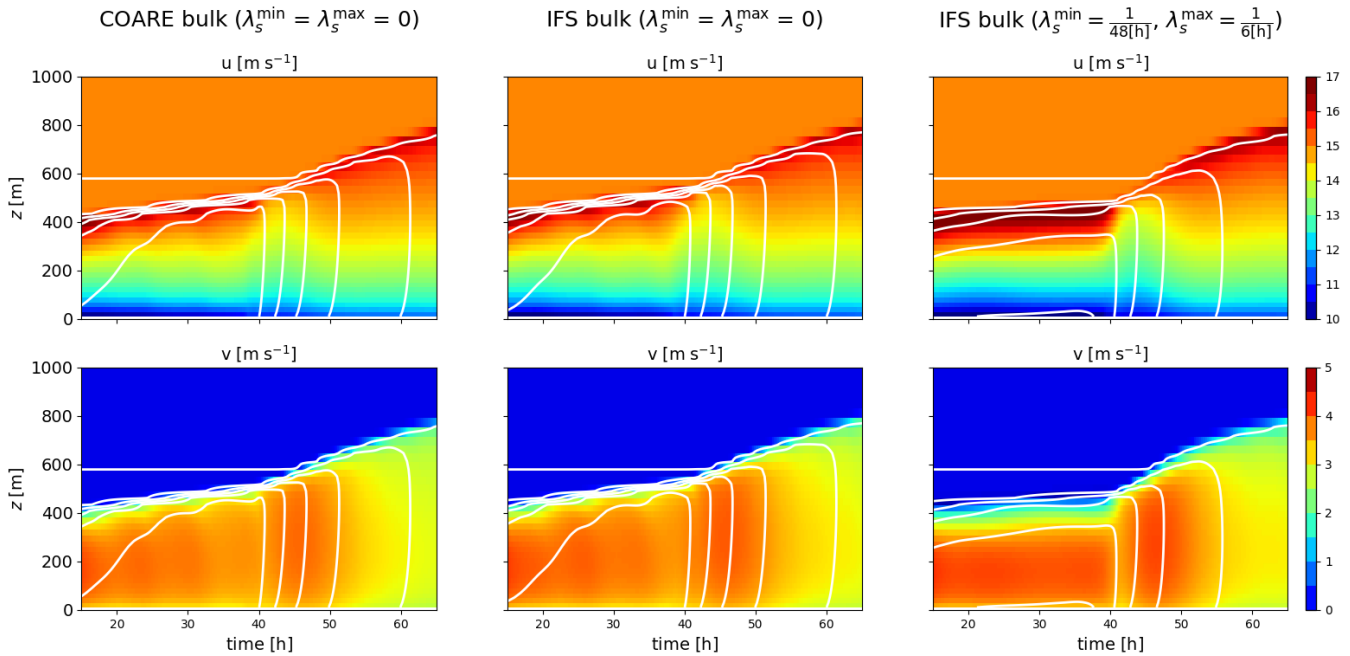
Figure 8. 2D time vs height sections representing the temporal evolution of the zonal (top panels) and meridional (bottom panels) components of atmospheric winds for ABL1d simulations of an air column crossing an SST front with COARE bulk formulation (left panels) and IFS bulk formulation (middle and right panels). For the case presented in the right panels, a Newtonian relaxation toward the initial temperature profile was added with $\lambda_s^{min} = \frac{1}{48[h]}$ and $\lambda_s^{max} = \frac{1}{6[h]}$. The simulations were performed with l_{D80} mixing length and CCH02 model constants.

the expected behaviour and we will focus the discussion on other options. In terms of zonal 10m wind the buoyancy based l_{BL89} and l_{D80} mixing lengths provide a good agreement with the MesoNH solution which could be expected as the MesoNH solution has been generated using the l_{BL89} mixing length. As soon as the mixing length is function of buoyancy and vertical
500 shear (as is the case for $l_{D80}^\star$) the simulated winds are weaker because the boundary layer is thinner. This leads to improved results in the stably stratified case shown earlier but in the present case more representative of realistic configuration in the MABL it leads to a too weak mixing. However, compared to the l_{R17} mixing length the $l_{D80}^\star$ still performs reasonably well but the winds on the warm side of the front are about $1\,\mathrm{m\,s^{-1}}$ weaker than the MesoNH winds for $c_0 = 0.15$ and become weaker and weaker as c_0 increases. For the last numerical experiments we will study, the l_{R17} mixing length will be discarded from
505 the comparison.

Although relevant for the present study this 2D x-z experiment is not fully representative of realistic conditions because the air column has time to adjust to the underlying oceanic state which is kept frozen in time.
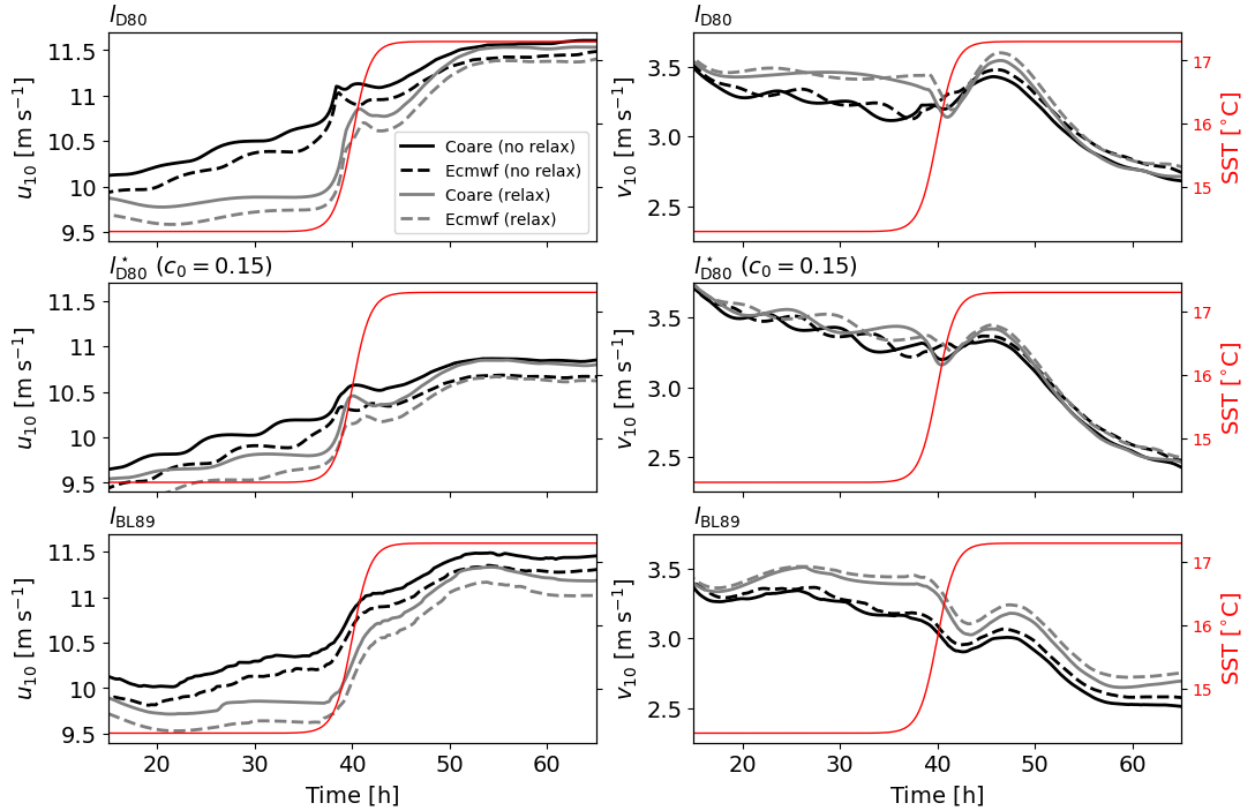
Figure 9. Temporal evolution of the zonal (left panels) and meridional (right panels) components of 10m atmospheric winds for ABL1d simulations of an air column crossing an SST front. The temporal evolution of SST (solid red lines) is also shown. For each panels the results from 4 different simulations are shown: with COARE bulk formulation (solid lines) or IFS bulk formulation (dashed lines), with Newtonian relaxation on temperature such that $\lambda_s^{\min} = \frac{1}{48[h]}$ and $\lambda_s^{\max} = \frac{1}{6[h]}$ (gray lines) or no relaxation (black lines). The top panels are obtained from simulations performed with l_{D80} mixing length, middle panels with $l_{\mathrm{D80}}^{\star}$ ($c_0 = 0.15$) and bottom l_{BL89}.

4.3.3 A single-column version

An alternative to the x-z setup would be to formulate the testcase as a Lagrangian advection of an air column over an SST front
510 by prescribing a temporal evolution of sea surface temperature $\theta_s(t)$ as

$$\theta_s(t) = 288.95 + 3 \left[\frac{1}{2} \tanh \left(\frac{3(t - 144 \times 10^3 \,\mathrm{s})}{20000} \right) \right], \qquad t \in [0, 80 \times 3600 \,\mathrm{s}]$$

In this case the air column does not necessarily have time to adjust to the underlying oceanic conditions. Initial conditions are the same as the ones of the 2D x-z case. For this testcase we do not have a reference solution but it is expected that the temporal evolution of the solution should be relatively similar to the spatial evolution in the MesoNH 2D x-z case studied in
515 previous subsection. This can be seen from Fig. 8 where there is a clear similarity between the time vs height sections obtained

with the ABL1d simulations and the x vs height sections shown for MesoNH in Fig. 6. The ABL1d solution shows a temporal lag analogous to the horizontal lag in the reference solution for the 2D x-z case. In addition to that, we also use this testcase to investigate the sensitivity of the solutions to the bulk formulation and to the Newtonian relaxation which was absent in simulations discussed so far. We consider the COARE and IFS bulk formulation which are relatively close to each other to
520   check the robustness of the results to small perturbations in surface fluxes. We also consider simulations with a relaxation of the temperature variable toward the initial condition with a fast restoring time scale $\lambda_s = \frac{1}{6[\mathrm{h}]}$ above the PBL and a slower one $\lambda_s = \frac{1}{48[\mathrm{h}]}$ in the PBL. This is meant to check that the relaxation does not completely overwrites the physics of the coupling we aim at representing with the ABL1d model. Results from those sensitivity experiments are shown in Fig. 8 and 9. In particular in Fig. 9 the evolution of the $10\,\mathrm{m}$ winds across the SST front closely resembles the one shown in Fig. 7 (dashed red lines) for
525   MesoNH. Moreover the results in Fig. 9 are robust to a change of bulk formulation to compute the surface fluxes. Reassuringly, adding a relaxation toward large-scale data which did not see the SST front does not deteriorate the realism of the solutions, as can be seen from Fig. 8 (rightmost panels) and 9 (gray lines).

Based on the results reported in this section, the best balance between efficiency and physical relevance is obtained when using the parameter values from CCH02 and the modified Deardorff (1980) mixing length formulation l_{D80} or $l_{\mathrm{D80}}^{\star}$.

530   ## 5   Coupled numerical experiments

In addition to idealized atmosphere-only simulations, we now show an illustration of the results obtained when the ABL1d model is coupled with NEMO to represent explicitly interactions between the upper ocean, sea-ice and the MABL. To do so, we performed a 5-years global simulation using the ORCA025 configuration. Details and illustrations are given hereafter.

5.1   Coupled NEMO-ABL1d configuration

535   We use here a global ORCA025 configuration at a $0.25°$ horizontal resolution (Barnier et al., 2006) with 75 vertical z-levels forced by ECMWF ERA-Interim 6-hours analysis (Dee et al., 2011). This configuration is identical to the one described in Couvelard et al. (2019) (see their Sec. 4.1.1). The ABL1d-NEMO coupled simulation is carried out with the same numerical options as in a standard ASL forcing strategy. However, in the ABL coupling strategy, the two-dimensional near-surface air temperature, humidity and winds used in the usual ASL forcing are replaced by three-dimensional atmospheric variables
540   sampled between the surface and $2000\,\mathrm{m}$ preprocessed following the different steps described in App. A. The large-scale pressure gradient computed during the preprocessing is used as a geostrophic forcing for the ABL1d model dynamics. Three-dimensional atmospheric variables are generated over the 2014-2018 period and vertically interpolated on 50 levels between $10\,\mathrm{m}$ and $2000\,\mathrm{m}$ with a vertical resolution increasing with height. Grid resolution is about $20\,\mathrm{m}$ near the air-sea interface and reaches $70\,\mathrm{m}$ at the top of the ABL1d domain. The choice of a vertical extent of $2000\,\mathrm{m}$ and 50 vertical levels in the ABL1d
545   model is somewhat arbitrary and the robustness of numerical results to these choices will be investigated in future studies. For the simulations presented here, same horizontal grid and time-step ($\Delta t = 1200\,\mathrm{s}$) are chosen in the ABL1d and NEMO models. The options associated with the ABL coupling available through the NEMO standard namelist are reported in Tab. 3.

Namelist parameter	Type	Description
ln_hpgls_frc	boolean	true if $\mathbf{R}_{\mathrm{LS}} = \left(\frac{1}{\rho_a}\nabla_h p\right)_{\mathrm{LS}}$ in (1)
ln_geos_winds	boolean	true if $\mathbf{R}_{\mathrm{LS}} = f\mathbf{k} \times \mathbf{u}_G$ in (1)
nn_dyn_restore	integer	(=0) no wind relaxation (=1) wind relaxation scaled by $r_{\mathrm{eq}}(f)$ as in (10) (=2) wind relaxation everywhere
rn_ldyn_min	real	inverse of λ_m^{max} in hours (see Sec. 2.4)
rn_ldyn_max	real	inverse of λ_m^{min} in hours (see Sec. 2.4)
rn_ltra_min	real	inverse of λ_s^{max} in hours (see Sec. 2.4)
rn_ltra_max	real	inverse of λ_s^{min} in hours (see Sec. 2.4)
nn_amxl	integer	(=0) l_{D80} mixing length (=1) $l_{\mathrm{D80}}^{\star}$ mixing length (=2) l_{BL89} mixing length (=3) l_{R17} mixing length
rn_Cm	real	C_m parameter in TKE scheme
rn_Ct	real	C_s parameter in TKE scheme
rn_Ce	real	C_e parameter in TKE scheme
rn_Ceps	real	c_ε parameter in TKE scheme
rn_Rod	real	c_0 parameter in $l_{\mathrm{D80}}^{\star}$ and l_{R17} mixing lengths
rn_Ric	real	C_1 parameter in the definition of ϕ_z
ln_smth_pblh	boolean	horizontal smoothing of PBL height

Table 3. Namelist parameters in the NEMO(v4.0) to set in the namelist section namsbc_abl before running a simulation coupled with ABL1d.

5.2 Numerical results

In this section, we evaluate the ABL coupling strategy in a realistic context for a set of relevant metrics. The objective is not
550 to conduct a thorough physical analysis of the numerical results but to illustrate the potential of the ABL coupling strategy and
its proper implementation in NEMO. To evaluate our numerical results, we use standard metrics from the literature to quantify
the wind/SST (a.k.a. thermal feedback effect), wind/currents (a.k.a. current feedback effect) and MABL/sea-ice couplings (e.g.
Bryan et al., 2010; Renault et al., 2019b). To quantify the surface wind response to SST, we show in Fig. 10 global maps
of the temporal correlation between the high-pass filtered $10\,\mathrm{m}$ wind speed from the first vertical level in the ABL1d model
555 and the SST. Same correlation is shown in Bryan et al. (2010) from satellite observations (their Fig. 1d) and from coupled
numerical experiments between a $0.1°$ ocean and a $0.25°$ atmospheric models (their Fig. 1c). Consistent with observations and
fully-coupled models, the correlation obtained from the coupled NEMO-ABL1d simulation shows large positive correlations
over regions like the Southern Ocean, Kuroshio and Gulf Stream extensions as well as in the Gulf of Guinea. Correlations are
however weaker than observations in the northern and equatorial Pacific between $90°\,\mathrm{W}$ and $180°\,\mathrm{W}$. As the thermal feedback
560 strength is related to the ocean model resolution (Bryan et al., 2010), we can expect a better agreement with observations using
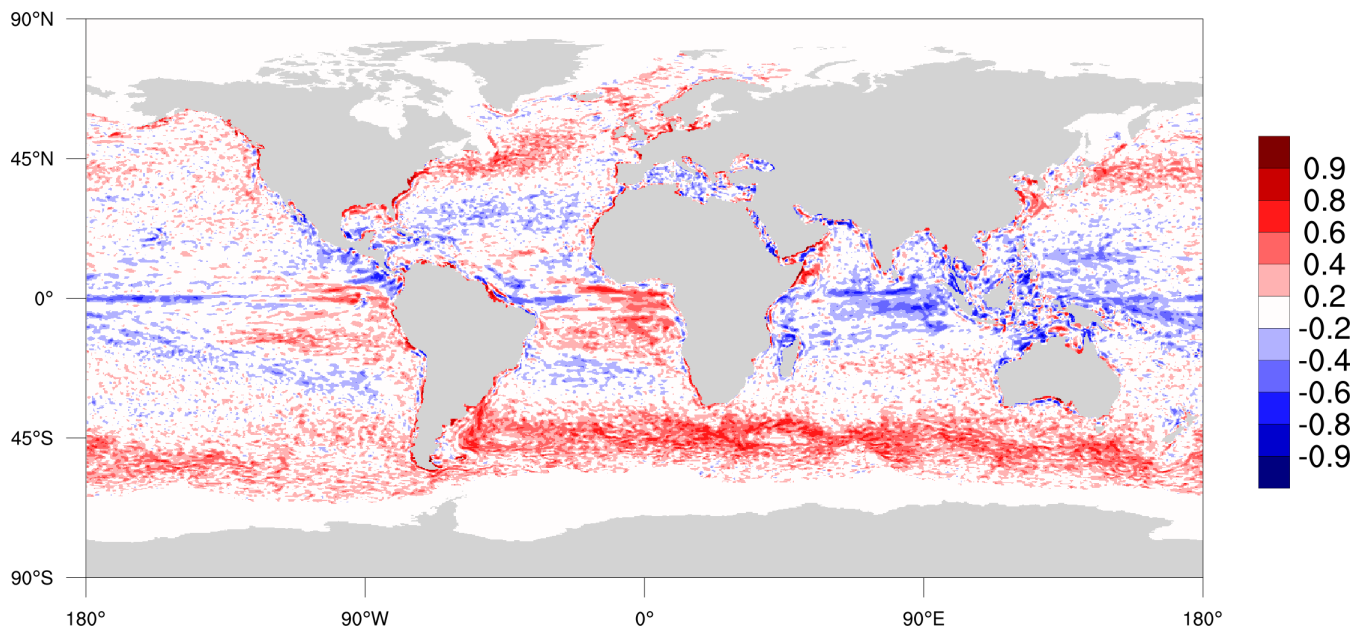
Figure 10. Global map of temporal correlation of high-pass filtered wind speed at the first vertical level of the ABL1d model with SST from NEMO. Both NEMO and ABL1d are configured at $0.25°$ resolution.

a higher resolution configuration such as ORCA12 ($1/12°$ resolution). This coupling sensitivity to the oceanic resolution will be addressed in a future study.

Other processes of interest are those related to the coupling between oceanic surface currents, wind-stress and wind. Such coupling is responsible for a dampening of the eddy mesoscale activity in the ocean. In Renault et al. (2019b), two coupling
565 coefficients called s_w and s_τ are defined to quantify this effect. s_τ is a measure of the sink of energy from the eddies and fronts to the ABL and s_w quantifies the partial re-energization of the ocean by the wind response to the wind/current coupling. This re-energization is absent in the ASL forcing strategy which results in an excessive dampening of the oceanic eddy mesoscale activity. In practice, s_τ (resp. s_w) corresponds to the slope of the linear relationship between high-pass filtered surface current vorticity and surface wind-stress (resp. wind) curl. Global maps of s_τ and s_w computed from our coupled NEMO-ABL1d
570 global simulation are shown in Fig. 11. Large negative values of s_τ indicate an efficient dampening of the eddy mesoscale activity by the current feedback (i.e. a large sink of energy from the ocean to the atmosphere) and the large positive values of s_w indicate an efficient wind response and re-energization of the mesoscale currents. Our numerical experiment provides results very consistent with the results obtained from coupled simulations between NEMO and the Weather and Research Forecasting model (WRF) shown in Renault et al. (2019b) (their Fig. 1b for s_τ and 2c for s_w). As mentioned earlier, with an
575 ASL forcing strategy we would systematically have $s_w = 0$ and stronger s_τ values.

The last illustration of our implementation presented in this section is the coupling of ABL1d with sea-ice. As described in Sec. 4.2, sea-ice generally induces a shallow stably stratified boundary layer due to the near-surface air cooling. This increased
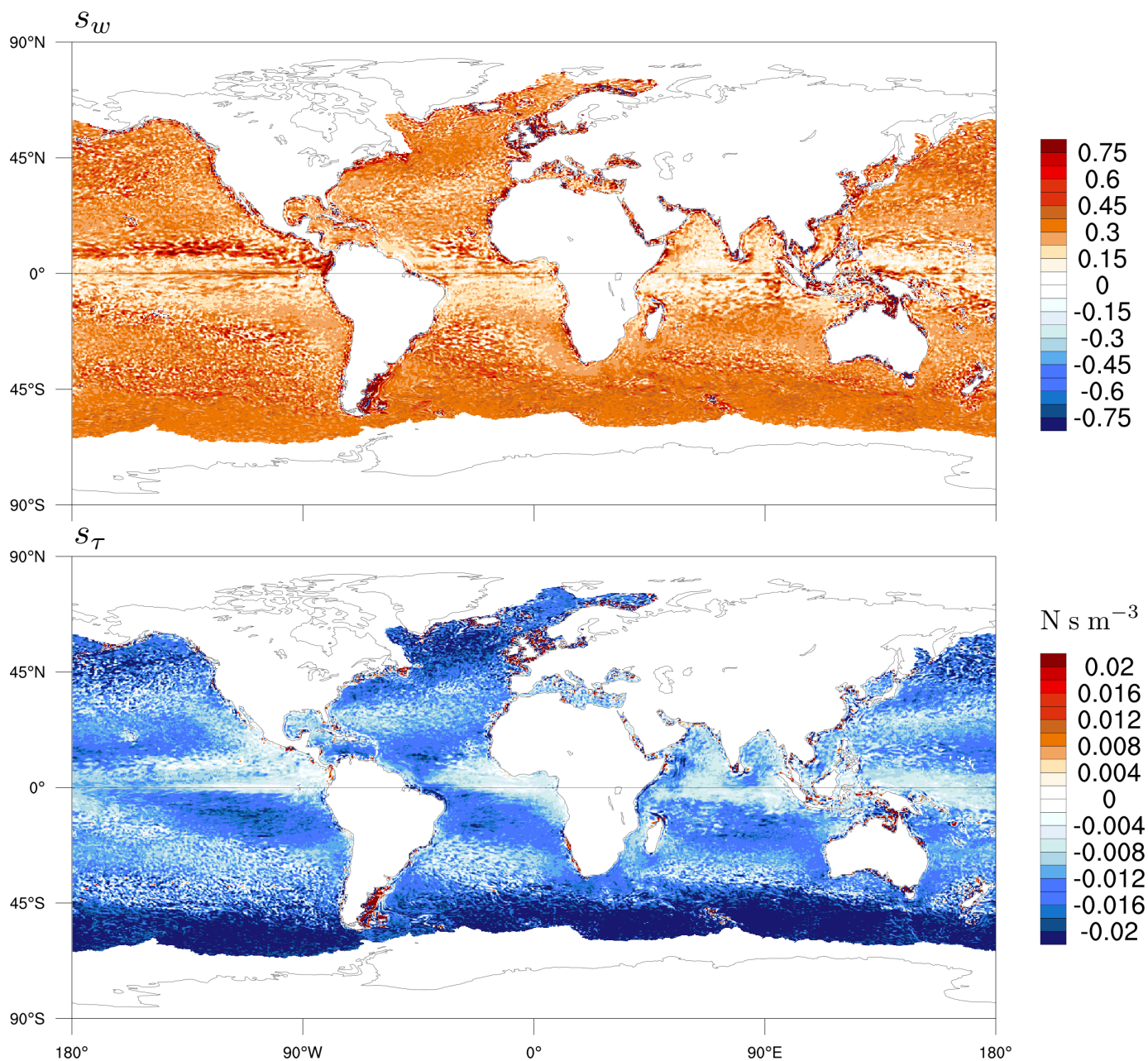
Figure 11. Global maps of the coupling coefficient between the surface current vorticity and the wind curl (s_w, top) and between the surface current vorticity and the wind-stress curl (s_τ, bottom) estimated from a $0.25°$ resolution coupled NEMO-ABL1d global simulation. The fields are first temporally averaged using a 29-day running mean and spatially high-pass filtered.
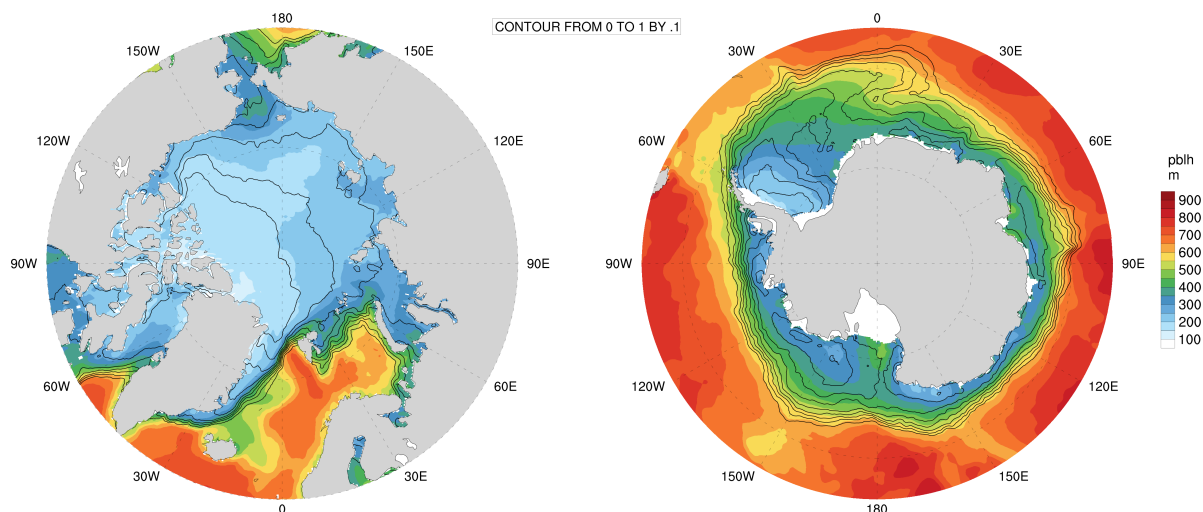
Figure 12. Yearly average of sea-ice cover (contours) and atmospheric boundary layer height (shaded) over the antarctic (right) and arctic (left) regions.

vertical stability tends to reduce atmospheric turbulence, producing shallower PBL heights over sea-ice. This relationship between sea-ice concentration and PBL height is clearly visible from Fig. 12 on both Arctic and Antarctic domains where the
580 ABL height follows a progressive decrease from about $800m$ to $200m$ in the transition zone between the open ocean and fully ice-covered regions. This coupling between the PBL and sea-ice have important effects on near-surface wind, temperature and humidity, and consequently on sea-ice concentration evolution which will need to be specifically assessed in future ABL-based studies.

5.3 Code performance and profiling

585 At this point in the manuscript, we anticipate that the interested reader has already wondered several times what could be the computational cost of the proposed methodology. To finalize our description of the implementation of this simplified atmospheric boundary layer model in NEMO, we assess the computational efficiency of our approach. We compare the performance of two simulations: one with a coupling with the ABL1d model (with 50 vertical levels) which requires reading 3D atmospheric data in input files, and one with a standard ASL forcing strategy which necessitates reading only 2D atmospheric data. For
590 the coupling with ABL1d, we consider the l_{D80} mixing length which gave robustly good results across the different numerical tests investigated earlier in the manuscript. The simulations are performed with NEMO version 4.0 for the ORCA025 configuration previously described on 128 cores (Intel(R) Xeon(R) E5 processors 2.6 GHz) compiled with ifort (v13.0.1) using the "$-i4 - r8 - O3 - fp - model\ precise - fno - alias$" options. The I/Os are handled via Lustre file system. Each MPI subdomain has 80×130 points in the horizontal and 75 points in the vertical. The various reports given below have been obtained
595 from a built-in NEMO code instrumentation dedicated to calculation measurement (e.g. Maisonnave and Masson, 2019). As mentioned earlier, the outputs are done using the parallel I/O capabilities provided by the XIOS library. Thanks to XIOS, we

do not expect any significant difference between the two simulations regarding the cost of output operations. However, the use of XIOS to handle input operations is still under development and because of the significant amount of data to read in the ABL coupling strategy, it makes sense to assess the associated overhead. We ran the ASL forced and ABL coupled NEMO simula-

600 tions for $20\,\mathrm{days}$ such that the cost of the initialization step is no longer visible in the averaged cost per time-step. Moreover, for the two simulations, the atmospheric data necessary for the computation of the turbulent components of air-sea fluxes are provided every $6\,\mathrm{hours}$.

We first show in Fig. 13 the elapsed time for each time-step over the first $48\,\mathrm{h}$ of the simulations with different ways to specify the surface fluxes. For most time-steps, the overhead associated with the ABL1d when using the l_{D80} mixing length

605 is very small (in the order of 4%), however every 18 time-steps (i.e. every 6 hours), there is a larger overhead due to the input part of the I/O operations. To further refine our assessment, we report in Tab. 4 the elapsed and CPU time spent on average over all the processors in the 11 most expansive sections of the code. As expected, the CPU time is not significantly affected by the ABL1d model (increase of 4%), but the elapsed time is increased by about 9% because of the time spent in waiting for I/O operations.

610 The overhead associated with input operations could be mitigated by reducing the number of vertical levels in the ABL1d model (we used 50 levels here to get an upper bound on the computational overhead) and either by using XIOS to handle input operations or by running ABL1d in detached mode as explained in Sec. 3.4 such that the time spent reading input files is covered by actual computations. Nonetheless the small increase in CPU time leaves room for further improvements of the ABL model to relax the horizontal homogeneity assumption.

615 **6 Conclusions**

A simplified atmospheric boundary layer (ABL) model has been developed and integrated to an oceanic model. This development is made with the objective to improve the representation of air-sea interactions in eddying oceanic models compared to the standard forcing strategy where the 10 meter height atmospheric quantities are prescribed. For this preliminary study, the simplified ABL model takes the form of a single column model including a turbulence scheme coupled to each oceanic grid point.

620 A crucial hypothesis is that the dominant process at the characteristic scale of the oceanic mesoscale is the so-called downward mixing process which stems from a modulation of atmospheric turbulence by sea surface temperature (SST) anomalies. Our approach can be seen as an extended bulk approach: instead of prescribing atmospheric quantities at 10 meters to compute air-sea fluxes via an atmospheric surface layer (ASL) parameterization, atmospheric quantities in the first few hundred meters are used to constrain an ABL model which provides 10 meter atmospheric values to the ASL parameterization. An important

625 point is that our modeling strategy keeps the computational efficiency and flexibility inherent to ocean only modeling.

In this paper the key components of such an approach have been described. This includes the large-scale forcing strategy, the coupling with the ocean and sea-ice and last but not least the ABL turbulence closure scheme based on a prognostic equation for the turbulence kinetic energy. The resulting simplified model, called ABL1d, has been tested for several boundary-layer regimes relevant to either ocean/atmosphere or sea-ice/atmosphere coupling. Results have systematically been evaluated
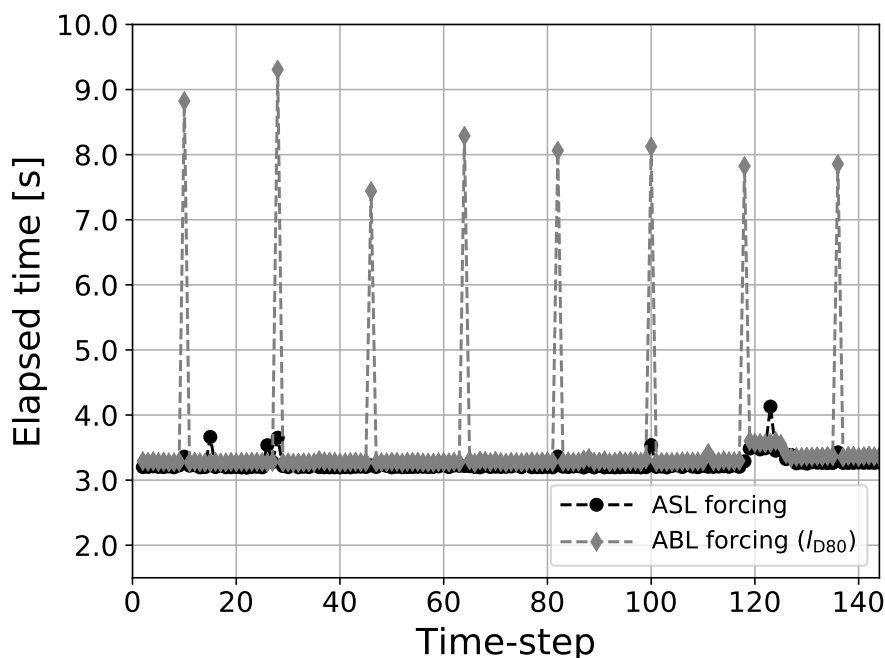
Figure 13. Elapsed time for each time-step of a 48 h simulation with standard ASL forcing strategy (black circles) and ABL forcing strategy using the l_{D80} mixing length (grey diamonds). For the two simulations the time-step size is $\Delta t = 1200$ s.

630   against Large Eddy Simulations (LES). Furthermore we have investigated the behaviour of the model to several parameters including the formulation of the mixing length and the turbulence model constants. First results from a global ABL1d-NEMO configuration show an excellent behaviour in term of wind-SST two-way coupling. A thorough analysis of the impact of the coupling with ABL1d from a physical viewpoint will be presented in subsequent work (e.g. Brivoal et al., 2020).

      Several ways to improve the methodology presented here are currently under investigation. The continuous formulation
635   of the ABL1d model will be completed by adding a mass-flux representation in our turbulent closure scheme and and by integrating the effect of horizontal advection and fine-scale pressure gradient. As mentioned several times in the paper ways to lower the computational overhead due to I/O inputs will be investigated. Moreover, following the work of Couvelard et al. (2019) it is planned to explicitly account for the effect of surface waves in the ABL coupling strategy.

      We wish to conclude this study by clarifying that the framework we have developed within NEMO is general enough to
640   allow alternative approaches (e.g. via model-driven empirical models) to be seamlessly tested and confronted with the ABL coupling strategy.

Section	ASL forcing		ABL coupling		Description
	Elapsed	CPU	Elapsed	CPU	
dyn_spg	789.2 s (15.22%)	786.5 s (15.42%)	778.2 s (13.79%)	775.5 s (14.62%)	Non-linear free surface
icedyn_rhg	637.9 s (12.30%)	639.2 s (12.53%)	634.7 s (11.24%)	638.6 s (12.04%)	Sea-ice rheology
tra_adv	623.9 s (12.03%)	613.8 s (12.04%)	626.0 s (11.09%)	615.9 s (11.61%)	3D tracer advection with FCT scheme
zdf_phy	546.6 s (10.54%)	545.4 s (10.70%)	541.0 s (9.59%)	538.8 s (10.16%)	Vertical physics: surface boundary layer + internal wave mixing
dyn_adv	229.1 s (4.42%)	227.9 s (4.47%)	229.2 s (4.06%)	227.9 s (4.30%)	3D Nonlinear momentum advection
tra_ldf	221.0 s (4.26%)	220.0 s (4.31%)	220.3 s (3.90%)	219.4 s (4.14%)	Isoneutral diffusion operator
ldf_slp	185.5 s (3.58%)	184.2 s (3.61%)	186.6 s (3.30%)	184.35 s (3.48%)	Computation of local neutral directions
dom_vvl	245.4 s (4.74%)	229.7 s (4.51%)	243.6 s (4.32%)	228.5 s (4.31%)	Lagrangian evolution of vertical scale factors with free surface
dyn_nxt	159.9 s (3.08%)	151.5 s (2.97%)	159.0 s (2.82%)	150.8 s (2.84%)	barotropic/baroclinic coupling and Asselin time filtering
dyn_zdf	131.8 s (2.54%)	131.3 s (2.57%)	130.8 s (2.32%)	130.3 s (2.46%)	Apply bottom and surface stress and solve the implicit vertical mixing
sbc	**101.6** s (1.96%)	**92.77** s (1.82%)	**580.8** s (10.29%)	**327.4** s (6.17%)	Surface flux computation (turbulent and non-turbulent)
…	…	…	…	…	
Total	5184.985 s	5099.884 s	5643.897 s	5302.949 s	

Table 4. Report of the elapsed time and CPU time in different sections of the NEMO(v4.0) code for the ASL forcing strategy (left portion of the table) and the ABL coupling strategy (right portion of the table). The timing is averaged on all processors. The right most column provides a quick description of the task handled by the corresponding section. On top of the timing in seconds the percentage of the total CPU and elapsed associated to each section is reported in parentheses. The computational overhead associated to the ABL coupling strategy can be estimated from the sbc section and the elapsed/CPU time.

Code and data availability. The changes to the NEMO code have been made on the standard NEMO code (release 4.0). The code can be
645 downloaded from the NEMO website (http://www.nemo-ocean.eu/, last access: 23 June 2020). The NEMO code modified to include the
ABL1d model is available in the zenodo archive (https://doi.org/10.5281/zenodo.3904518, Lemarié and Samson (2020)). The namelists and
data used to produce the figures are also available in the zenodo archive.

Appendix A: Preprocessing of atmospheric data from IFS

A1 Altitude of IFS vertical levels

The ABL1d model is discretized on fixed in time and space geopotential levels while the IFS model uses a pressure-based sigma coordinate. A first step is to recover the altitude associated with each sigma level. The pressure $p_{k+\frac{1}{2}}$ defined at cell interfaces between two successive vertical layers is given by

$$p_{k+\frac{1}{2}} = A_{k+\frac{1}{2}} + B_{k+\frac{1}{2}} p_s, \qquad k \in [\![1, N_{\mathrm{ifs}}]\!]$$

where $A_{k+\frac{1}{2}}$ (Pa) and $B_{k+\frac{1}{2}}$ (dimensionless) are constants given by a smooth analytical function defining the vertical grid stretching. Typical values of the altitude of grid points in the vertical for a standard 60 levels grid (L60) and a surface pressure of $1013\,\mathrm{hPa}$ are given in Tab. A1.

Once the values of $p_{k+\frac{1}{2}}$ and p_s are known, the altitude of cell interfaces can be computed by integrating the hydrostatic equilibrium

$$\partial_z \phi = -\frac{R_d T_v}{p} \partial_z p \qquad\qquad\qquad\qquad\qquad\qquad\qquad\text{(A1)}$$

vertically. In (A1), ϕ is the geopotential, T_v the virtual temperature and R_d the specific gas constant for dry air. At a discrete level we get

$$\int_{z_{k-\frac{1}{2}}}^{z_{k+\frac{1}{2}}} \partial_s \phi \, ds = -R_d T_v(z_k) \int_{z_{k-\frac{1}{2}}}^{z_{k+\frac{1}{2}}} \left(\frac{\partial_s p}{p} \right) ds$$

which gives

$$\mathrm{e3t}_k^{\mathrm{ifs}} = -\frac{R_d T_v(z_k)}{g} \ln\left(\frac{p_{k+\frac{1}{2}}}{p_{k-\frac{1}{2}}} \right)$$

Once the the layer thicknesses $\mathrm{e3t}_k^{\mathrm{ifs}}$ are known, horizontal wind components, potential temperature and specific humidity can be interpolated on the ABL1d vertical levels. Under the constraint that $\int_{z_{\mathrm{sfc}}}^{z_{\mathrm{top}}} \psi^{\mathrm{ifs}}(z) \, \mathrm{d}z = \int_{z_{\mathrm{sfc}}}^{z_{\mathrm{top}}} \psi(z) \, \mathrm{d}z$ for any IFS quantity ψ^{ifs} to be interpolated. Wind components are interpolated using a fourth-order compact scheme while tracers are interpolated using a WENO-like PPM scheme (A. Shchepetkin, personal communication) which is monotonic.

A2 Filtering in the presence of boundaries

Because of the IFS numerical formulation and of the post-processing of output data, the solutions sometimes contain high frequency oscillations at the vicinity of the land-sea interface. This problem is further compounded when the nearshore topography is steep. The atmospheric fields over water thus need to be smoothed horizontally to specifically remove the $2\Delta x$ noise.

Index	A_k [Pa]	B_k	Altitude z_k [m]	Layer thickness $\text{e3t}_k^{\text{cep}}$ [m]
1	0.000000	1.000000	10.00	20.00
2	0.000000	0.997630	34.97	29.94
3	7.367743	0.994019	71.89	43.92
4	65.889244	0.988270	124.48	61.30
5	210.393890	0.979663	195.85	81.49
6	467.333588	0.967645	288.55	104.01
7	855.361755	0.951822	404.72	128.43
8	1385.912598	0.931940	546.06	154.40
9	2063.779785	0.907884	713.97	181.61
10	2887.696533	0.879657	909.57	209.81
11	3850.913330	0.847375	1133.73	238.78
12	4941.778320	0.811253	1387.12	268.33
13	6144.314941	0.771597	1670.26	298.31
14	7438.803223	0.728786	1983.49	328.58

Table A1. Altitude z_k and layer thickness e3t_k of the IFS L60 vertical grid in the first 2000 meters with respect to the parameter values A_k and B_k of a surface pressure $p_s = 1013$ hPa.

675 We use a standard two-dimensional Shapiro filter which, in the absence of lateral boundaries, can be formulated as

$$\psi_{i,j}^{\star} = \psi_{i,j} + \frac{1}{4}\left(\delta_{i+1/2,j}^{(x)} - \delta_{i-1/2,j}^{(x)}\right)$$
$$\psi_{i,j}^{\text{f}} = \psi_{i,j}^{\star} + \frac{1}{4}\left(\delta_{i,j+1/2}^{(y,\star)} - \delta_{i,j-1/2}^{(y,\star)}\right)$$

where $\delta_{i+1/2,j}^{(x)} = \psi_{i+1,j} - \psi_{i,j}$ and $\delta_{i,j+1/2}^{(y,\star)} = \psi_{i,j+1}^{\star} - \psi_{i,j}^{\star}$. The amplification factor associated to this filter is

$$\mathcal{A}_{\text{shap}}(\theta_x, \theta_y) = \frac{1}{4}\left(1 + \cos\theta_x\right)\left(1 + \cos\theta_y\right), \qquad \theta_x = k_x\Delta x, \quad \theta_y = k_y\Delta y$$

680 which guarantees that one iteration of the filter is sufficient to remove the grid-scale noise since $\mathcal{A}_{\text{shap}}(\pi,\pi) = \mathcal{A}_{\text{shap}}(\pi,\theta_y) = \mathcal{A}_{\text{shap}}(\theta_x,\pi) = 0$ and that $\mathcal{A}_{\text{shap}} \leq 1$ (i.e. no waves are amplified). In the presence of solid boundaries we would like to retain those properties as much as possible. A straightforward approach would be to impose a no-gradient condition at the coast, i.e. $\delta_{i+1/2,j}^{(x)} = 0$ as soon as $\text{tmask}_{i+1,j} \times \text{tmask}_{i,j} = 0$ (resp. $\delta_{i,j+1/2}^{(y,\star)} = 0$ as soon as $\text{tmask}_{i,j+1} \times \text{tmask}_{i,j} = 0$) with tmask the indicator function equal to 1 over water and 0 over land. Let us also consider the following alternative boundary conditions

$$
685 \quad \begin{cases} \delta_{i+1/2,j}^{(x)} = -\delta_{i-1/2,j}^{(x)}, & \text{if } \text{tmask}_{i+1,j} = 0 \\ \delta_{i-1/2,j}^{(x)} = -\delta_{i+1/2,j}^{(x)}, & \text{if } \text{tmask}_{i-1,j} = 0 \end{cases} \tag{A2}
$$

and similar in the y-direction. We do not elaborate on this choice but it can be shown theoretically that boundary conditions (A2) provide a better control of grid-scale noise near the coast. To illustrate this point, in Fig. A1 the surface pressure gradients
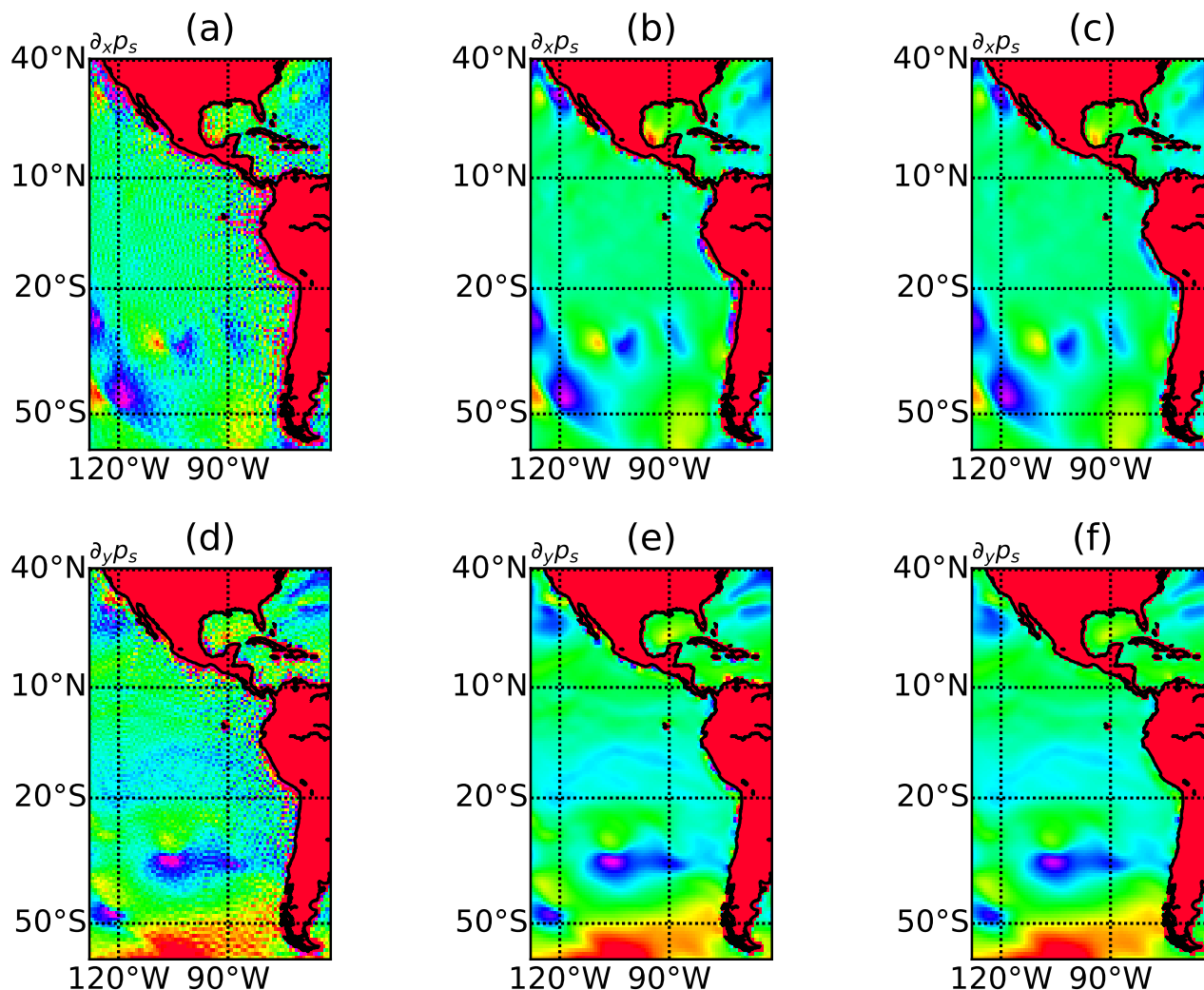
Figure A1. Atmospheric surface pressure horizontal gradients in x (top panels) and y (bottom panels) directions obtained from the original IFS data (a and d), after a Shapiro filtering with no gradient boundary conditions (b and e), and after a Shapiro filtering with boundary conditions (A2) (c and f). The area in red is covered by land.

are shown for different boundary conditions. In particular it can be seen near the coast that the no gradient boundary condition (panels b and e) leaves some artifical patterns in gradients especially in the Peru-Chile current system while boundary condition (A2) efficiently mitigate this issue. Note that it is particularly essential to make sure that the surface pressure field is sufficiently smooth because gradients of this field are used to compute geostrophic winds which are important for the large-scale forcing of the ABL1d model.

A3 Large-scale pressure gradient computation

The last aspect of the pre-processing of atmospheric data we would like to discuss is the computation of the large-scale pressure

695   gradient (or equivalently of the geostrophic wind components) The objective is to estimate the following terms

$$R_{\mathrm{LS}}^u = \frac{1}{\rho_a}(\partial_x p)_z, \qquad R_{\mathrm{LS}}^v = \frac{1}{\rho_a}(\partial_y p)_z,$$

where $(\cdot)_z$ denotes a gradient along constant geopotential height. Using the hydrostatic balance we have $\frac{1}{\rho_a} = -g(\partial_z p)^{-1}$ which leads to

$$R_{\mathrm{LS}}^u = -g(\partial_z p)^{-1}(\partial_x p)_z, \qquad R_{\mathrm{LS}}^v = -g(\partial_z p)^{-1}(\partial_y p)_z \qquad (A3)$$

700   Assuming a generalized vertical coordinate $s = s(x,y)$ the computation of gradients along constant height is not straightforward since $(\partial_x p)_z = (\partial_x p)_s - (\partial_z p)(\partial_x z)_s$ leading to

$$(\partial_x p)_z (\partial_z p)^{-1} = (\partial_z p)^{-1}(\partial_x p)_s - (\partial_x z)_s$$

In the particular case of the IFS coordinate s we have

$$(\partial_z p)^{-1}(\partial_x p)_s = \frac{B(z)\partial_x p_s}{(\partial_z A) + (\partial_z B)p_s} \qquad (A4)$$

705   and $(\partial_x z)_s$ can be estimated after integrating the hydrostatic balance.

Starting from the layer interfaces height $z_{i,j,k+1/2}^{\mathrm{ifs}}$, surface pressure $(p_s)_{i,j}$ and parameter values $A_k, B_k, A_{k+1/2}, B_{k+1/2}$ the different steps are the following:

1. Compute $\Delta x_{i,j}$ and $\Delta y_{i,j}$ from latitudes and longitudes

2. Compute horizontal gradients $\partial_x p_s$ and $\partial_y p_s$ for surface pressure

710 $$\mathrm{FX}_{i+1/2,j} = \frac{2\left\{(p_s)_{i+1,j} - (p_s)_{i,j}\right\}}{\Delta x_{i,j} + \Delta x_{i+1,j}}, \qquad \mathrm{FY}_{i,j+1/2} = \frac{2\left\{(p_s)_{i,j+1} - (p_s)_{i,j}\right\}}{\Delta y_{i,j} + \Delta y_{i,j+1}}$$

3. Compute horizontal gradients $(\partial_x z)_s$ and $(\partial_y z)_s$

$$\mathrm{dZx}_{i+1/2,j,k} = \frac{z_{i+1,j,k+1/2}^{\mathrm{cep}} - z_{i,j,k+1/2}^{\mathrm{cep}} + z_{i+1,j,k-1/2}^{\mathrm{cep}} - z_{i,j,k-1/2}^{\mathrm{cep}}}{\Delta x_{i,j} + \Delta x_{i+1,j}}$$

$$\mathrm{dZy}_{i,j+1/2,k} = \frac{z_{i,j+1,k+1/2}^{\mathrm{cep}} - z_{i,j,k+1/2}^{\mathrm{cep}} + z_{i,j+1,k-1/2}^{\mathrm{cep}} - z_{i,j,k-1/2}^{\mathrm{cep}}}{\Delta y_{i,j} + \Delta y_{i,j+1}}$$

4. Compute $(\partial_z p)^{-1}(\partial_x p)_s$ via (A4)

715 $$\mathrm{wrkX}_{i,j,k} = \frac{1}{2} \frac{B_k\left(z_{i,j,k+1/2}^{\mathrm{cep}} - z_{i,j,k-1/2}^{\mathrm{cep}}\right)\left(\mathrm{FX}_{i+1/2,j} + \mathrm{FX}_{i-1/2,j}\right)}{(p_s)_{i,j}(B_{k+1/2} - B_{k-1/2}) + (A_{k+1/2} - A_{k-1/2})}$$

$$\mathrm{wrkY}_{i,j,k} = \frac{1}{2} \frac{B_k\left(z_{i,j,k+1/2}^{\mathrm{cep}} - z_{i,j,k-1/2}^{\mathrm{cep}}\right)\left(\mathrm{FY}_{i+1/2,j} + \mathrm{FY}_{i-1/2,j}\right)}{(p_s)_{i,j}(B_{k+1/2} - B_{k-1/2}) + (A_{k+1/2} - A_{k-1/2})}$$

5. Finalize (we get a minus sign in R_{LS}^u because the grid in the y-direction is flipped in the raw data)

$$
\begin{aligned}
(R_{\mathrm{LS}}^u)_{i,j,k} &= -g\left(\mathrm{wrkY}_{i,j,k} - \frac{1}{2}(\mathrm{dZy}_{i,j+1/2,k} + \mathrm{dZy}_{i,j-1/2,k})\right) \\
(R_{\mathrm{LS}}^v)_{i,j,k} &= -g\left(\mathrm{wrkX}_{i,j,k} - \frac{1}{2}(\mathrm{dZx}_{i+1/2,j,k} + \mathrm{dZx}_{i-1/2,j,k})\right)
\end{aligned}
$$

720 *Author contributions.* Florian Lemarié has written the paper with the help of all the coauthors. Florian Lemarié, Guillaume Samson, and Gurvan Madec designed and developed a preliminary version of the ABL1d model within NEMO 3.6 stable version. This original code was then ported to NEMO release 4.0. Jean-Luc Redelsperger and Hervé Giordani have provided inputs in the design of the TKE closure scheme and of the numerical experiments. Florian Lemarié has carried out the idealized numerical experiments, Guillaume Samson the realistic experiments and Jean-Luc Redelsperger the MesoNH simulations.

725 *Competing interests.* The authors declare that they have no conflict of interest.

Acknowledgements. Florian Lemarié, Guillaume Samson, and Gurvan Madec have received funding from the European Union's Horizon 2020 research and innovation programme under grant agreement No 821926 (IMMERSE). Florian Lemarié and Jean-Luc Redelsperger also acknowledge the support by Mercator-Ocean and the Copernicus Marine Environment Monitoring Service (CMEMS) through contract 730 22-GLO-HR - Lot 2 (High-resolution ocean, waves, atmosphere interaction).

References

Andren, A., Brown, A. R., Mason, P. J., Graf, J., Schumann, U., Moeng, C.-H., and Nieuwstadt, F. T. M.: Large-eddy simulation of a neutrally stratified boundary layer: A comparison of four computer codes, Quart. J. Roy. Meteorol. Soc., 120, 1457–1484, 1994.

Ayet, A. and Redelsperger, J.-L.: An analytical study of the atmospheric boundary layer flow and divergence over a SST front, Quart. J. Roy. Meteorol. Soc., https://doi.org/10.1002/qj.3578, 2019.

Barnier, B., Siefridt, L., and Marchesiello, P.: Thermal forcing for a global ocean circulation model using a three-year climatology of ECMWF analyses, J. Mar. Res., 6, 363 – 380, https://doi.org/https://doi.org/10.1016/0924-7963(94)00034-9, 1995.

Barnier, B., Madec, G., Penduff, T., Molines, J.-M., Treguier, A.-M., Le Sommer, J., Beckmann, A., Biastoch, A., Böning, C., Dengg, J., Derval, C., Durand, E., Gulev, S., Remy, E., Talandier, C., Theetten, S., Maltrud, M., McClean, J., and De Cuevas, B.: Impact of partial steps and momentum advection schemes in a global ocean circulation model at eddy-permitting resolution, Ocean Dyn., 56, 543–567, https://doi.org/10.1007/s10236-006-0082-1, https://doi.org/10.1007/s10236-006-0082-1, 2006.

Bazile, E., Marquet, P., Bouteloup, Y., and Bouyssel, F.: The Turbulent Kinetic Energy (TKE) scheme in the NWP models at Meteo France, in: Workshop on Workshop on Diurnal cycles and the stable boundary layer, 7-10 November 2011, pp. 127–135, ECMWF, ECMWF, Shinfield Park, Reading, https://www.ecmwf.int/node/8006, 2012.

Beljaars, A., Dutra, E., Balsamo, G., and Lemarié, F.: On the numerical stability of surface–atmosphere coupling in weather and climate models, Geosci. Model Dev., 10, 977–989, 2017.

Beljaars, A. C. M.: The parametrization of surface fluxes in large-scale models under free convection, Quart. J. Roy. Meteorol. Soc., 121, 255–270, 1995.

Bielli, S., Douville, H., and Pohl, B.: Understanding the West African monsoon variability and its remote effects: An illustration of the grid point nudging methodology, Clim. Dynam., 35, 159–174, https://doi.org/10.1007/s00382-009-0667-8, 2009.

Bougeault, P. and Lacarrère, P.: Parameterization of orography-induced turbulence in a mesobeta-scale model, Mon. Weather Rev., 117, 1872–1890, 1989.

Brivoal, T., Samson, G., Giordani, H., Bourdallé-Badie, R., Lemarié, F., and Madec, G.: Impacts of the currents feedback on upper kinetic energy over the North-East Atlantic from a coupled ocean atmospheric boundary layer model, Ocean Sci., under review, 2020.

Brodeau, L., Barnier, B., Gulev, S. K., and Woods, C.: Climatologically Significant Effects of Some Approximations in the Bulk Parameterizations of Turbulent Air–Sea Fluxes, J. Phys. Oceanogr., 47, 5–28, https://doi.org/10.1175/JPO-D-16-0169.1, 2017.

Bryan, F. O., Tomas, R., Dennis, J. M., Chelton, D. B., Loeb, N. G., and McClean, J. L.: Frontal Scale Air–Sea Interaction in High-Resolution Coupled Climate Models, J. Climate, 23, 6277–6291, https://doi.org/10.1175/2010JCLI3665.1, 2010.

Burchard, H.: Energy-conserving discretisation of turbulent shear and buoyancy production, Ocean Modell., 4, 347 – 361, https://doi.org/https://doi.org/10.1016/S1463-5003(02)00009-4, http://www.sciencedirect.com/science/article/pii/S1463500302000094, 2002a.

Burchard, H.: Applied Turbulence Modelling in Marine Waters, Lecture Notes in Earth Sciences, Springer Berlin Heidelberg, 2002b.

Businger, J. and Shaw, W.: The response of the marine boundary layer to mesoscale variations in sea-surface temperature, Dynam. Atmos. Oceans, 8, 267–281, 1984.

Cavaleri, L., Fox-Kemper, B., and Hemer, M.: Wind Waves in the Coupled Climate System, Bull. Amer. Meteor. Soc., 93, 1651–1661, https://doi.org/10.1175/BAMS-D-11-00170.1, 2012.

Chelton, D. B. and Xie, S.-P.: Coupled ocean-atmosphere interaction at oceanic mesoscales, Oceanogr., 23, 52–69, 2010.

Cheng, Y., Canuto, V. M., and Howard, A. M.: An improved model for the turbulent PBL, J. Atmos. Sci., 59, 1550–1565, 2002.

Couvelard, X., Lemarié, F., Samson, G., Redelsperger, J.-L., Ardhuin, F., Benshila, R., and Madec, G.: Development of a 2-way coupled
770   ocean-wave model: assessment on a global NEMO(v3.6)-WW3(v6.02) coupled configuration, Geosci. Model Dev. Disc., 2019, 1–36,
        https://doi.org/10.5194/gmd-2019-189, https://www.geosci-model-dev-discuss.net/gmd-2019-189/, 2019.

Craig, A., Valcke, S., and Coquart, L.: Development and performance of a new version of the OASIS coupler, OASISMCT3.0, Geosci. Model
        Dev., 10, 3297–3308, https://doi.org/10.5194/gmd-10-3297-2017, 2017.

Cuxart, J., Bougeault, P., and Redelsperger, J.-L.: A turbulence scheme allowing for mesoscale and large-eddy simulations, Quart. J. Roy.
775   Meteorol. Soc., 126, 1–30, 2000.

Cuxart, J., Holtslag, A. A. M., Beare, R. J., Bazile, E., Beljaars, A., Cheng, A., Conangla, L., Ek, M., Freedman, F., Hamdi, R., Kerstein,
        A., Kitagawa, H., Lenderink, G., Lewellen, D., Mailhot, J., Mauritsen, T., Perov, V., Schayes, G., Steeneveld, G.-J., Svensson, G., Taylor,
        P., Weng, W., Wunsch, S., and Xu, K.-M.: Single-Column Model Intercomparison for a Stably Stratified Atmospheric Boundary Layer,
        Bound.-Lay. Meteorol., 118, 273–303, 2006.

780 Deardorff, J. W.: Three-dimensional numerical study of turbulence in an entraining mixed layer, Bound.-Lay. Meteorol., 7, 199–226, 1974.

Deardorff, J. W.: Stratocumulus-capped mixing layers derived from a three dimensional model, Bound.-Lay. Meteorol., 18, 495–527, 1980.

Dee, D. P., Uppala, S. M., Simmons, A. J., Berrisford, P., Poli, P., Kobayashi, S., Andrae, U., Balmaseda, M. A., Balsamo, G., Bauer,
        P., Bechtold, P., Beljaars, A. C. M., van de Berg, L., Bidlot, J., Bormann, N., Delsol, C., Dragani, R., Fuentes, M., Geer, A. J., Haim-
        berger, L., Healy, S. B., Hersbach, H., Hólm, E. V., Isaksen, L., Kållberg, P., Köhler, M., Matricardi, M., McNally, A. P., Monge-Sanz,
785   B. M., Morcrette, J.-J., Park, B.-K., Peubey, C., de Rosnay, P., Tavolato, C., Thépaut, J.-N., and Vitart, F.: The ERA-Interim reanalysis:
        configuration and performance of the data assimilation system, Quarterly Journal of the Royal Meteorological Society, 137, 553–597,
        https://doi.org/10.1002/qj.828, 10.1002/qj.828, 2011.

Deleersnijder, E., Beckers, J.-M., Campin, J.-M., El Mohajir, M., Fichefet, T., and Luyten, P.: Some mathematical problems associated with
        the development and use of marine models, in: The Mathematics of Models for Climatology and Environment, edited by Díaz, J. I., pp.
790   39–86, Springer Berlin Heidelberg, Berlin, Heidelberg, 1997.

Deremble, B., Wienders, N., and Dewar, W. K.: CheapAML: A Simple, Atmospheric Boundary Layer Model for Use in Ocean-Only Model
        Calculations, Mon. Weather Rev., 141, 809–821, 2013.

Deshayes, J., Tréguier, A.-M., Barnier, B., Lecointre, A., Sommer, J. L., Molines, J.-M., Penduff, T., Bourdallé-Badie, R., Drillet, Y., Garric,
        G., Benshila, R., Madec, G., Biastoch, A., Böning, C. W., Scheinert, M., Coward, A. C., and Hirschi, J. J.-M.: Oceanic hindcast simulations
795   at high resolution suggest that the Atlantic MOC is bistable, J. Geophys. Res., 40, 3069–3073, https://doi.org/doi:10.1002/grl.50534,
        wOS:000321951300034, 2013.

Dewar, W. K. and Flierl, G. R.: Some Effects of the Wind on Rings, J. Phys. Oceanogr., 17, 1653–1667, 1987.

Frenger, I., Gruber, N., Knutti, R., and Munnich, M.: Southern Ocean Eddies Affect Local Weather, Nature Geosci., 6, 608–612, 2013.

Giordani, H., Planton, S., Bénech, B., and Kwon, B.-H.: Atmospheric boundary layer response to sea surface temperatures during the
800   Semaphore experiment, J. Geophys. Res., 103, 25 047–25 060, 1998.

Giordani, H., Caniaux, G., and Prieur, L.: A Simplified 3D Oceanic Model Assimilating Geostrophic Currents: Application to the POMME
        Experiment, J. Phys. Oceanogr., 35, 628–644, https://doi.org/10.1175/JPO2724.1, 2005.

Haney, R. L.: Surface Thermal Boundary Condition for Ocean Circulation Models, J. Phys. Oceanogr., 1, 241–248,
        https://doi.org/10.1175/1520-0485(1971)001<0241:STBCFO>2.0.CO;2, 1971.

805   Hogg, A., Dewar, W., Berloff, P., Kravtsov, S., and Hutchinson, D. K.: The effects of mesoscale ocean-atmosphere coupling on the large-scale
ocean circulation, J. Climate, 22, 4066–4082, 2009.

Hourdin, F., Couvreux, F., and Menut, L.: Parameterization of the Dry Convective Boundary Layer Based on a Mass Flux Representation of
Thermals, J. Atmos. Sci., 59, 1105–1123, https://doi.org/10.1175/1520-0469(2002)059<1105:POTDCB>2.0.CO;2, 2002.

Kilpatrick, T., Schneider, N., and Qiu, B.: Boundary Layer Convergence Induced by Strong Winds across a Midlatitude SST Front, J. Climate,
810   27, 1698–1718, 2014.

Lac, C., Chaboureau, J.-P., Masson, V., Pinty, J.-P., Tulet, P., Escobar, J., Leriche, M., Barthe, C., Aouizerats, B., Augros, C., Aumond, P.,
Auguste, F., Bechtold, P., Berthet, S., Bielli, S., Bosseur, F., Caumont, O., Cohard, J.-M., Colin, J., Couvreux, F., Cuxart, J., Delautier,
G., Dauhut, T., Ducrocq, V., Filippi, J.-B., Gazen, D., Geoffroy, O., Gheusi, F., Honnert, R., Lafore, J.-P., Lebeaupin Brossier, C., Libois,
Q., Lunet, T., Mari, C., Maric, T., Mascart, P., Mogé, M., Molinié, G., Nuissier, O., Pantillon, F., Peyrillé, P., Pergaud, J., Perraud, E.,
815   Pianezze, J., Redelsperger, J.-L., Ricard, D., Richard, E., Riette, S., Rodier, Q., Schoetter, R., Seyfried, L., Stein, J., Suhre, K., Taufour,
M., Thouron, O., Turner, S., Verrelle, A., Vié, B., Visentin, F., Vionnet, V., and Wautelet, P.: Overview of the Meso-NH model version 5.4
and its applications, Geosci. Model Dev., 11, 1929–1969, https://doi.org/10.5194/gmd-11-1929-2018, 2018.

Lafore, J. P., Stein, J., Asencio, N., Bougeault, P., Ducrocq, V., Duron, J., Fischer, C., Héreil, P., Mascart, P., Masson, V., Pinty, J. P.,
Redelsperger, J. L., Richard, E., and Vilà-Guerau de Arellano, J.: The Meso-NH Atmospheric Simulation System. Part I: adiabatic formu-
820   lation and control simulations, Ann. Geophys., 16, 90–109, 1998.

Lambaerts, J., Lapeyre, G., Plougonven, R., and Klein, P.: Atmospheric response to sea surface temperature mesoscale structures, J. Geophys.
Res., 118, 9611–9621, 2013.

Large, W. G.: Surface Fluxes for Practitioners of Global Ocean Data Assimilation, in: Ocean Weather Forecasting. An Integrated View of
Oceanography, edited by Chassignet, E. P. and Verron, J., chap. 9, pp. 229–270, Springer, 2006.

825   Large, W. G. and Yeager, S. G.: The global climatology of an interannually varying air-sea flux data set, Clim. Dynam., 33, 341–364,
https://doi.org/10.1007/s00382-008-0441-3, 2009.

Lemarié, F., Blayo, E., and Debreu, L.: Analysis of Ocean-atmosphere Coupling Algorithms: Consistency and Stability, Procedia Com-
puter Science, 51, 2066 – 2075, https://doi.org/https://doi.org/10.1016/j.procs.2015.05.473, http://www.sciencedirect.com/science/article/
pii/S1877050915012818, international Conference On Computational Science, ICCS 2015, 2015.

830   Lemarié, F. and Samson, G.: A simplified atmospheric boundary layer model for an improved representation of air-sea interactions in eddying
oceanic models: implementation and first evaluation in NEMO (v4.0)), https://doi.org/10.5281/zenodo.3904518, 2020.

Lemarié, F., Kurian, J., Shchepetkin, A. F., Molemaker, M. J., Colas, F., and McWilliams, J. C.: Are there in-
escapable issues prohibiting the use of terrain-following coordinates in climate models?, Ocean Modell., 42, 57 – 79,
https://doi.org/https://doi.org/10.1016/j.ocemod.2011.11.007, http://www.sciencedirect.com/science/article/pii/S1463500311001831,
835   2012.

Lilly, D.: The representation of small-scale turbulence in numerical simulation experiments, In Proc. IBM Sci. Comput. Symp. on Environ-
mental Sci., Nov. 14–16, 1966, Thomas J. Watson Res. Center, Yorktown Heights, N. Y., IBM Form 320–1951, pp. 195–210, 1967.

Lindzen, R. S. and Nigam, S.: On the role of sea surface temperature gradients in forcing low-level winds and convergence in the tropics, J.
Atmos. Sci., 44, 2418–2436, 1987.

840   Madec, G.: NEMO ocean engine, in: Note du Pole de modélisation No. 27, Institut Pierre-Simon Laplace (IPSL), France, 2012.

Maisonnave, E. and Masson, S.: Ocean/sea-ice macro task parallelism in NEMO, in: Technical report, TR/GMGC/15/54, available at http:
//www.nemo-ocean.eu/content/download/167787/683246/file/opa_sas_tr.pdf, 2015.

Maisonnave, E. and Masson, S.: NEMO 4.0 performance: how to identify and reduce unnecessary communications, in: Technical report, TR/CMGC/19/19, available at https://cerfacs.fr/wp-content/uploads/2019/01/GLOBC-TR_Maisonnave-Nemo-2019.pdf, 2019.

845 Marchesiello, P., Capet, X., Menkes, C., and Kennan, S.: Submesoscale dynamics in tropical instability waves, Ocean Modell., 39, 31–46, https://doi.org/10.1016/j.ocemod.2011.04.011, 2011.

McWilliams, J. C., Gula, J., and Molemaker, M. J.: The Gulf Stream North Wall: Ageostrophic Circulation and Frontogenesis, J. Phys. Oceanogr., 49, 893–916, https://doi.org/10.1175/JPO-D-18-0203.1, 2019.

Metzger, E. J., Smedstad, O. M., Thoppil, P. G., Hurlburt, H. E., Cummings, J. A., Wallcraft, A. J., Zamudio, L., Franklin, D. S., Posey,
850 P. G., Phelps, M. W., Hogan, P. J., Bub, F. L., and DeHaan, C. J.: US Navy Operational Global Ocean and Arctic Ice Prediction Systems, Oceanogr., 27, https://doi.org/10.5670/oceanog.2014.66, 2014.

Meurdesoif, Y., Caubel, A., Lacroix, R., Dérouillat, J., and Nguyen, M.: XIOS Tutorial, available at http://forge.ipsl.jussieu.fr/ioserver/raw-attachment/wiki/WikiStart/XIOS-tutorial.pdf, 2016.

Minobe, S., Kuwano-Yoshida, A., Komori, N., Xie, S.-P., and Small, R. J.: Influence of the Gulf Stream on the troposphere, Nature, pp.
855 206–209, 2008.

Monin, A. S. and Obukhov, A. M.: Basic laws of turbulent mixing in the surface layer of the atmosphere, Trudy Akademii Nauk SSSR Geofizicheskogo Instituta, 24, 163–187, 1954.

Mulholland, D. P., Laloyaux, P., Haines, K., and Balmaseda, M. A.: Origin and Impact of Initialization Shocks in Coupled Atmosphere-Ocean Forecasts, Mon. Weather Rev., 143, 4631–4644, https://doi.org/10.1175/MWR-D-15-0076.1, 2015.

860 Oerder, V., Colas, F., Echevin, V., Masson, S., Hourdin, C., Jullien, S., Madec, G., and Lemarié, F.: Mesoscale SST–wind stress coupling in the Peru–Chile current system: Which mechanisms drive its seasonal variability?, Clim. Dynam., pp. 1–22, 2016.

Oerder, V., Colas, F., Echevin, V., Masson, S., and Lemarié, F.: Impacts of the Mesoscale Ocean-Atmosphere Coupling on the Peru-Chile Ocean Dynamics: The Current-Induced Wind Stress Modulation, J. Geophys. Res., 123, 812–833, https://doi.org/10.1002/2017JC013294, https://agupubs.onlinelibrary.wiley.com/doi/abs/10.1002/2017JC013294, 2018.

865 Pelletier, C., Lemarié, F., and Blayo, E.: Sensitivity analysis and metamodels for the bulk parametrization of turbulent air–sea fluxes, Quart. J. Roy. Meteorol. Soc., 144, 658–669, https://doi.org/10.1002/qj.3233, 2018.

Razavi, S., Tolson, B. A., and Burn, D. H.: Review of surrogate modeling in water resources, Water Resour. Res., 48, https://doi.org/10.1029/2011WR011527, https://agupubs.onlinelibrary.wiley.com/doi/abs/10.1029/2011WR011527, 2012.

Redelsperger, J. L., Mahé, F., and Carlotti, P.: A Simple And General Subgrid Model Suitable Both For Surface Layer And Free-Stream
870 Turbulence, Bound.-Lay. Meteorol., 101, 375–408, 2001.

Redelsperger, J. L., Bouin, M. N., Pianezze, J., Garnier, V., and Marié, L.: Impact of a sharp, small-scale SST front on the marine atmospheric boundary layer on the Iroise Sea: analysis from a hectometric simulation, Quart. J. Roy. Meteorol. Soc., https://doi.org/10.1002/qj.3650, 2019.

Renault, L., Molemaker, M. J., Gula, J., Masson, S., and McWilliams, J. C.: Control and Stabilization of the Gulf Stream by Oceanic Current
875 Interaction with the Atmosphere, J. Phys. Oceanogr., 46, 3439–3453, https://doi.org/10.1175/JPO-D-16-0115.1, 2016a.

Renault, L., Molemaker, M. J., McWilliams, J. C., Shchepetkin, A. F., Lemarié, F., Chelton, D., Illig, S., and Hall, A.: Modulation of Wind Work by Oceanic Current Interaction with the Atmosphere, J. Phys. Oceanogr., 46, 1685–1704, 2016b.

Renault, L., Lemarié, F., and Arsouze, T.: On the implementation and consequences of the oceanic currents feedback in ocean–atmosphere coupled models, Ocean Modell., 141, 101 423, https://doi.org/https://doi.org/10.1016/j.ocemod.2019.101423, http://www.sciencedirect.
880 com/science/article/pii/S1463500319300459, 2019a.

Renault, L., Masson, S., Oerder, V., Jullien, S., and Colas, F.: Disentangling the Mesoscale Ocean-Atmosphere Interactions, J. Geophys. Res., 124, 2164–2178, https://doi.org/10.1029/2018JC014628, 2019b.

Rodier, Q., Masson, V., Couvreux, F., and Paci, A.: Evaluation of a Buoyancy and Shear Based Mixing Length for a Turbulence Scheme, Front. in Earth Sci., 5, 65, https://doi.org/10.3389/feart.2017.00065, https://www.frontiersin.org/article/10.3389/feart.2017.00065, 2017.

885 Rotta, J.: Statistische theorie nichthomogener turbulenz, Zeitschrift fur Physik, 129 (6), 547–572, 1951.

Rousset, C., Vancoppenolle, M., Madec, G., Fichefet, T., Flavoni, S., Barthélemy, A., Benshila, R., Chanut, J., Levy, C., Masson, S., and Vivier, F.: The Louvain-La-Neuve sea ice model LIM3.6: global and regional capabilities, Geosci. Model Dev., 8, 2991–3005, https://doi.org/10.5194/gmd-8-2991-2015, https://www.geosci-model-dev.net/8/2991/2015/, 2015.

Schneider, N. and Qiu, B.: The Atmospheric Response to Weak Sea Surface Temperature Fronts, J. Atmos. Sci., 72, 3356–3377,
890 https://doi.org/10.1175/JAS-D-14-0212.1, 2015.

Scire, J. S., Robe, F., Fernau, M., and Yamartino, R.: A user's guide for the CALMET meteorological model (Version 5), Tech. rep., Earth Tech: Concord, MA, USA, 2000.

Seager, R., Blumenthal, M. B., and Kushnir, Y.: An advective atmospheric mixed layer model for ocean modeling purposes: global simulation of surface heat fluxes, J. Climate, 8, 1952–1964, 1995.

895 Soares, P. M. M., Miranda, P. M. A., Siebesma, A. P., and Teixeira, J.: An eddy-diffusivity/mass-flux parametrization for dry and shallow cumulus convection, Quart. J. Roy. Meteorol. Soc., 130, 3365–3383, https://doi.org/10.1256/qj.03.223, 2004.

Spall, M.: Midlatitude Wind Stress–Sea Surface Temperature Coupling in the Vicinity of Oceanic Fronts, J. Climate, 20, https://doi.org/10.1175/JCLI4234.1, 2007.

Takano, K., Mintz, Y., and Han, J.-Y.: Numerical simulation of the world ocean circulation, Second Conf. on Numerical Weather Prediction,
900 Monterey, CA, Amer. Meteor. Soc., pp. 121–129, 1973.

Troen, I. B. and Mahrt, L.: A simple model of the atmospheric boundary layer; sensitivity to surface evaporation, Bound.-Lay. Meteorol., 37, 129–148, https://doi.org/10.1007/BF00122760, 1986.

von Schuckmann, K., Traon, P.-Y. L., Smith, N., Pascual, A., Brasseur, P., Fennel, K., Djavidnia, S., Aaboe, S., Fanjul, E. A., Autret, E., Axell, L., Aznar, R., Benincasa, M., Bentamy, A., Boberg, F., Bourdallé-Badie, R., Nardelli, B. B., Brando, V. E., Bricaud, C., Breivik,
905 L.-A., Brewin, R. J., Capet, A., Ceschin, A., Ciliberti, S., Cossarini, G., de Alfonso, M., de Pascual Collar, A., de Kloe, J., Deshayes, J., Desportes, C., Drévillon, M., Drillet, Y., Droghei, R., Dubois, C., Embury, O., Etienne, H., Fratianni, C., Lafuente, J. G., Sotillo, M. G., Garric, G., Gasparin, F., Gerin, R., Good, S., Gourrion, J., Grégoire, M., Greiner, E., Guinehut, S., Gutknecht, E., Hernandez, F., Hernandez, O., Høyer, J., Jackson, L., Jandt, S., Josey, S., Juza, M., Kennedy, J., Kokkini, Z., Korres, G., Kõuts, M., Lagemaa, P., Lavergne, T., le Cann, B., Legeais, J.-F., Lemieux-Dudon, B., Levier, B., Lien, V., Maljutenko, I., Manzano, F., Marcos, M., Marinova,
910 V., Masina, S., Mauri, E., Mayer, M., Melet, A., Mélin, F., Meyssignac, B., Monier, M., Müller, M., Mulet, S., Naranjo, C., Notarstefano, G., Paulmier, A., Gomez, B. P., Gonzalez, I. P., Peneva, E., Perruche, C., Peterson, K. A., Pinardi, N., Pisano, A., Pardo, S., Poulain, P.-M., Raj, R. P., Raudsepp, U., Ravdas, M., Reid, R., Rio, M.-H., Salon, S., Samuelsen, A., Sammartino, M., Sammartino, S., Sandø, A. B., Santoleri, R., Sathyendranath, S., She, J., Simoncelli, S., Solidoro, C., Stoffelen, A., Storto, A., Szerkely, T., Tamm, S., Tietsche, S., Tinker, J., Tintore, J., Trindade, A., van Zanten, D., Vandenbulcke, L., Verhoef, A., Verbrugge, N., Viktorsson, L., von Schuckmann, K.,
915 Wakelin, S. L., Zacharioudaki, A., and Zuo, H.: Copernicus Marine Service Ocean State Report, J. Oper. Oceanogr., 11, S1–S142, 2018.

Wallace, J. M., Mitchell, T. P., and Deser, C.: The Influence of Sea-Surface Temperature on Surface Wind in the Eastern Equatorial Pacific: Seasonal and Interannual Variability, J. Climate, 2, 1492–1499, https://doi.org/10.1175/1520-0442(1989)002<1492:TIOSST>2.0.CO;2, 1989.

Wilson, J. M. and Venayagamoorthy, S. K.: A Shear-Based Parameterization of Turbulent Mixing in the Stable Atmospheric Boundary Layer,

920   J. Atmos. Sci., 72, 1713–1726, https://doi.org/10.1175/JAS-D-14-0241.1, 2015.